JOURNAL OF PETROLOGY | VOLUME 46 | NUMBER 8 | PAGES 1689–1724 | 2005 | doi:10.1093/petrology/egi031

Microchemical and Sr Isotopic Investigation of Zoned K-feldspar Megacrysts: Insights into the Petrogenesis of a Granitic System and Disequilibrium Crystal Growth

D. GAGNEVIN[1]*, J. S. DALY[1], G. POLI[2] AND D. MORGAN[3]

[1]DEPARTMENT OF GEOLOGY, UNIVERSITY COLLEGE DUBLIN, BELFIELD, DUBLIN 4, IRELAND

[2]DEPARTMENT OF EARTH-SCIENCES, PIAZZA UNIVERSITÁ, 06100 PERUGIA, ITALY

[3]DEPARTMENT OF GEOLOGICAL SCIENCES, UNIVERSITY OF DURHAM, SOUTH ROAD, DURHAM DH1 3LE, UK

RECEIVED SEPTEMBER 25, 2003; ACCEPTED MARCH 1, 2005
ADVANCE ACCESS PUBLICATION APRIL 15, 2005

K-feldspar megacrysts (Kfm) are used to investigate the magmatic evolution of the 7 Ma Monte Capanne (MC) monzogranite (Elba, Italy). Dissolution and regrowth of Kfm during magma mixing or mingling events produce indented resorption surfaces associated with high Ba contents. Diffusion calculations demonstrate that Kfm chemical zoning is primary. Core-to-rim variations in Ba, Rb, Sr, Li and P support magma mixing (i.e. high Ba and P and low Rb/Sr at rims), but more complex variations require other mechanisms. In particular, we show that disequilibrium growth (related to variations in diffusion rates in the melt) may have occurred as a result of thermal disturbance following influx of mafic magma in the magma chamber. Initial $^{87}Sr/^{86}Sr$ ratios (I_{Sr}) (obtained by microdrilling) decrease from core to rim. Inner core analyses define a mixing trend extending towards a high I_{Sr}–Rb/Sr melt component, whereas the outer cores and rims display a more restricted range of I_{Sr}, but a larger range of Rb/Sr. Lower I_{Sr} at the rim of one megacryst suggests mixing with high-K calc-alkaline mantle-derived volcanics of similar age on Capraia. Trace element and isotopic profiles suggest (1) early megacryst growth in magmas contaminated by crust and refreshed by high I_{Sr} silicic melts (as seen in the inner cores) and (2) later recharge with mafic magmas (as seen in the outer cores) followed by (3) crystal fractionation, with possible interaction with hydrothermal fluids (as seen in the rim). The model is compatible with the field occurrence of mafic enclaves and xenoliths.

KEY WORDS: *Elba; monzogranite; K-feldspar megacrysts; zoning; magma mixing; trace element; Sr isotopes; petrogenesis*

INTRODUCTION

Since the pioneering work of Davidson *et al.* (1990), micro-scale isotopic variations within magmatic minerals have been increasingly used to investigate the evolution of complex magmatic systems subject to open-system behaviour (e.g. Feldstein *et al.*, 1994; Cox *et al.*, 1996; Davidson & Tepley, 1997; Davidson *et al.*, 1998, 2001; Knesel *et al.* 1999; Tepley *et al.*, 1999, 2000; Wolff *et al.*, 1999; Waight *et al.*, 2000*a*, 2000*b*, 2001; Halama *et al.*, 2002; Perini *et al.*, 2003; Tepley & Davidson, 2003). Through their zonation patterns, phenocrysts preserve an individual record of their environment during their growth. For example, zoned plagioclase phenocrysts have been extensively used to monitor processes such as magma mixing and crustal contamination (e.g. Davidson & Tepley, 1997). In these studies, microsampling (using drilling methods) followed by precise thermal ionization mass spectrometry (TIMS) Sr isotopic analyses (rarely Nd isotopes, e.g. Waight *et al.*, 2000*a*, 2000*b*) is the prime method, although laser ablation inductively coupled plasma mass spectrometry (ICP-MS) techniques are increasingly used, for both Sr (e.g. Davidson *et al.*, 2001) and Pb (e.g. Gagnevin *et al.*, 2005) isotopic analyses. As a result of crystal–melt diffusive equilibration, it is important to assess whether the isotopic zonation in phenocrysts truly represents the composition of the melt at each increment of growth (i.e. growth zoning) (e.g. Knesel *et al.* 1999; Tepley *et al.*, 1999, 2000). This may be

*Corresponding author. Telephone: (+353) 1 716 2138. Fax: (+353) 1 2837733. E-mail: Damien.Gagnevin@ucd.ie

achieved through coupled trace element studies (e.g. Halama *et al.*, 2002).

'Crystal isotopic stratigraphy' (Davidson *et al.*, 1998) has been successfully applied mostly to plagioclase phenocrysts in recent (<1 Ma) volcanic systems, but plutonic rocks have received much less attention. This arises from the fact that in plutonic rocks the primary isotopic zoning of individual mineral phases may be modified or lost altogether as a result of interaction with hydrothermal and/or meteoric fluids, and/or diffusional exchange during slow cooling. An important limitation in dealing with older and, especially, plutonic rocks is that uncertainties in the age cause significant uncertainties in the calculated initial isotopic composition owing to radiogenic growth. However, several investigations have overcome these difficulties. Cox *et al.* (1996) have shown that K-feldspar megacrysts in the Shap granite (England) preserve magmatic dissolution textures, Ba zoning and variations in Sr isotopic composition. Waight *et al.* (2000*b*, 2001) demonstrated that feldspar phenocrysts (from S-type granites and a gabbro–diorite complex, respectively) preserve internal isotopic heterogeneity and record various magma recharge events, including recharge with mantle-derived melts. Based on plagioclase isotopic zonation, Tepley & Davidson (2003) have shown that extensive crustal contamination occurred in the genesis of the Rum ultrabasic intrusion. Based on the extent of isotopic re-equilibration between melts and crystals, Tepley & Davidson (2003) also better constrained the cooling rate of the intrusion.

The Monte Capanne (MC) pluton (Elba Island, Italy), one of the youngest granitoids exposed on Earth (*c.* 7 Ma), provides compelling field, petrographic, geochemical and isotopic evidence for magma mixing (*sensu lato*) involving contrasting mantle- and crustal-derived components (e.g. Giraud *et al.*, 1986; Poli *et al.*, 1989; Bussy, 1991; Poli, 1992; Dini *et al.*, 2002; Gagnevin *et al.*, 2004). Mafic microgranular enclaves (MME) occur throughout the intrusion and provide convincing evidence for iterative magma mixing or mingling (Didier & Barbarin, 1991, and references therein). Disequilibrium textures displayed by plagioclase phenocrysts in MME (Gagnevin *et al.*, 2004) and reaction micro-textures between accessory minerals in the host monzogranite (Dini *et al.*, 2004) argue for a complex magma mixing history.

Feldstein *et al.* (1994) have shown that magma mixing between sub-crustal and mantle-derived magmas is responsible for large Sr isotopic variations (initial $^{87}Sr/^{86}Sr = 0{\cdot}7087–0{\cdot}7247$) in various minerals from the San Vincenzo volcanics in the Tuscan Magmatic Province (Fig. 1). Similarly, we want to refine whole-rock models for the evolution of the MC monzogranite (e.g. Dini *et al.*, 2002; Gagnevin *et al.*, 2004) using zoned K-feldspar megacrysts. These preserve evidence of resorption and regrowth (Daly & Poli, 1999), similar to those encountered in the Shap granite (Cox *et al.*, 1996). Zoned K-feldspar has been used in several cases (Knesel *et al.*, 1999; Perini *et al.*, 2003; Ginibre *et al.*, 2004) to validate magma mixing as a major process during petrogenesis.

In this study, we show conclusively that, through their petrography, chemical (major and trace elements) and Sr isotopic zoning, K-feldspar megacrysts in the Monte Capanne pluton (Tuscan Magmatic Province; Fig. 1) are indicators of magma mixing following various recharge events with felsic and mafic magmas. We also show that disequilibrium partitioning, partly caused by kinetic effects at the crystal–melt interface, can affect the trace element distribution over a large distance (i.e. *c.* 1 mm) of K-feldspar growth.

GEOLOGICAL BACKGROUND

The Tuscan Magmatic Province

Geodynamic evolution of the Northern Tyrrhenian Domain

The magmatism of the Tuscan Magmatic Province (TMP) (Fig. 1) is classically considered to be contemporaneous with the opening of the Tyrrhenian Sea (late Miocene) during back-arc extension following the collision and subduction of the Adriatic below the Corsica–Sardinia microplates (Principi & Treves, 1984; Serri *et al.*, 1993). The continuous eastward migration of deformation from Corsica to the Appeninic frontal thrust led to crustal thickening, syn-orogenic exhumation and post-orogenic extension in a back-arc setting (e.g. Jolivet *et al.*, 1998). The associated eastward migration of the magmatism is attributed to asthenospheric upwelling as a result of eastward roll-back and retreat of the Adriatic slab (Serri *et al.*, 1993; Jolivet *et al.* 1998).

Timing, location and nature of magmatism

Magmatism in the TMP mostly consists of anatectic acidic magmas (e.g. Taylor & Turi, 1976; Giraud *et al.*, 1986) with associated mantle-derived basic and intermediate magmas with potassic affinities (Poli *et al.*, 1984). Acidic intrusive rocks (8–6·3 Ma, Elba intrusive complex, Dini *et al.*, 2002) (Fig. 1), together with lamproitic activity in Corsica (14 Ma) constitute the early manifestations of the TMP, whereas trachydacites and high-K latites at Monte Amiata (Fig. 1) are the latest erupted products (318–190 ka; Ferrari *et al.*, 1996). Plutonic bodies occur on Elba Island (MC pluton *c.* 7 Ma; granite porphyries *c.* 8–7·4 Ma; Porto Azzuro pluton *c.* 5 Ma), Giglio Island (5 Ma) Montecristo Island (*c.* 7 Ma), Gavoranno (4·4–4·9 Ma) and in boreholes at Campiglia (4·3–5·7 Ma) (Fig. 1) (Ferrara & Tonarini, 1985; Westerman *et al.*, 1993; Innocenti *et al.*, 1997). Coeval mafic volcanism occurred on Capraia Island (7·6–4·7 Ma; Aldighieri *et al.*, 1998) (Fig. 1) and comprises high-K andesites and subordinate shoshonitic basalts. Subvolcanic rocks with

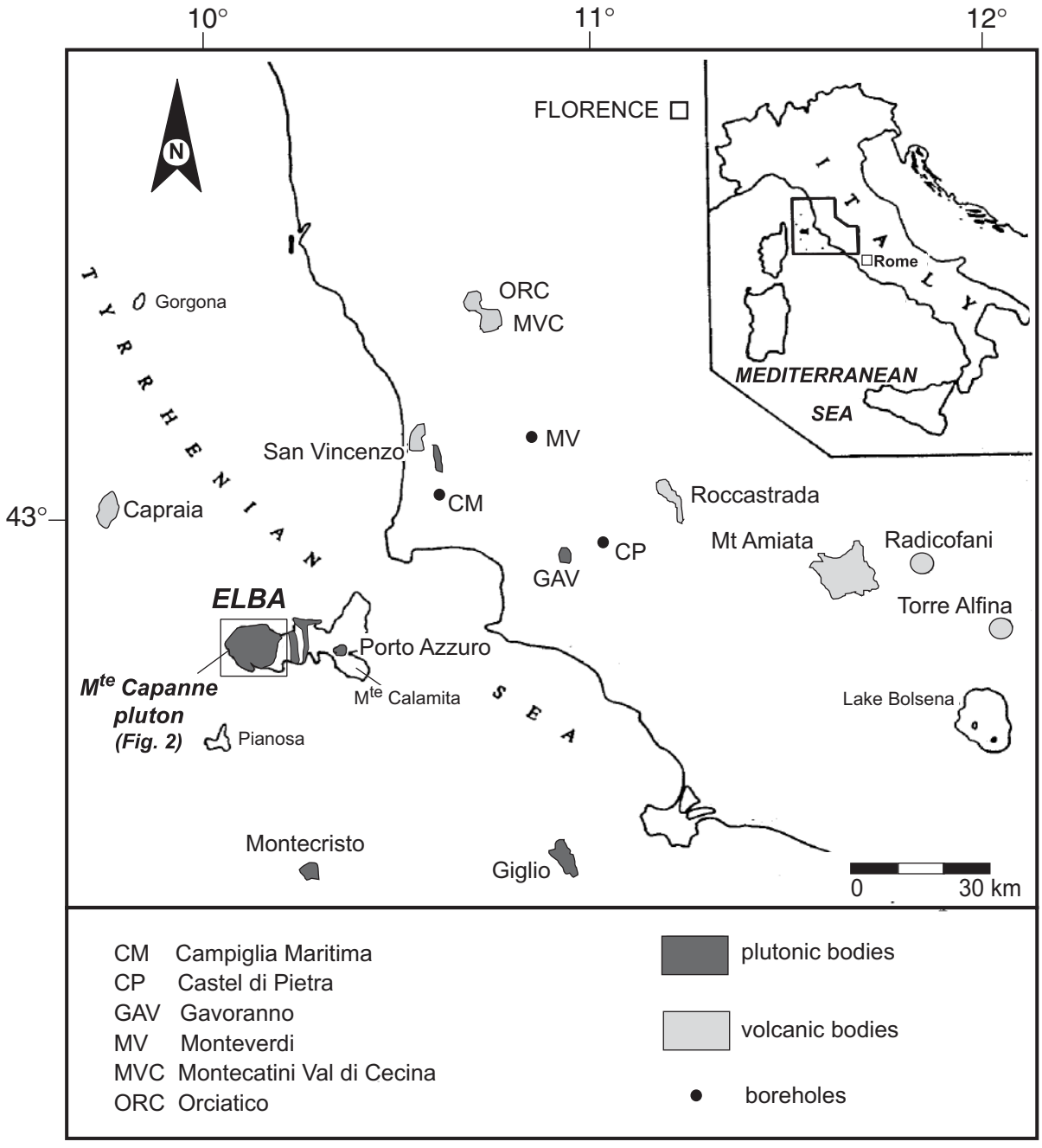

Fig. 1. Sketch map showing the location of the Monte Capanne pluton in relation to other components of the Tuscan Magmatic Province. Inset shows the location of the main map in Italy [modified after Hall *et al.* (1991)].

lamproitic affinities (e.g. orendites) also occur in Orciatico and Montecatini Val di Cecina at 4·1 Ma (Peccerillo *et al.*, 1988) (Fig. 1). Rhyolites occurred relatively late compared with the intrusive rocks and are found in the San Vincenzo (*c.* 4·4 Ma, Feldstein *et al.*, 1994), Tofla–Cerveteri–Manziana (*c.* 3·5 Ma; Ferrara *et al.*, 1988) and Roccastrada (2·4–3·2 Ma, Ferrara & Tonarini, 1985) volcanic centres (Fig. 1).

Previous geochemical studies

The TMP is classically considered to have a predominantly crustal signature through repeated melting of the heterogeneous Tuscan basement (Dupuy & Allègre, 1972; Taylor & Turi, 1976). However, the involvement of mantle-derived magmas in the genesis of the Tuscan magmas has been extensively described in both intrusive and extrusive rocks of the TMP, giving rise to a great

variety of hybrid products (Giraud *et al.*, 1986; Ferrara *et al.*, 1989; Poli *et al.*, 1989; Innocenti *et al.*, 1992, 1997; Poli, 1992; Serri *et al.*, 1993; Westerman *et al.*, 1993; Dini *et al.*, 2002). However, the exact nature of the multiple end-members involved in the genesis of the Tuscan hybrid magmas is still controversial. The mantle-derived end-member involved in the hybridization process is regarded to oscillate in composition between high-K calc-alkaline (e.g. occurring in Capraia Island; Poli, 1992; Dini *et al.*, 2002; Poli *et al.*, 2002) and lamproitic (e.g. Peccerillo *et al.*, 1988; Conticelli *et al.*, 1992) magmas. The Sr and Nd isotopic signature of San Vincenzo mafic enclaves is amongst the most primitive recorded in the TMP (Ferrara *et al.*, 1989). The heterogeneous nature of the mantle below the Italian peninsula is largely responsible for producing different primary melt compositions. In particular, the role of mantle metasomatism, inherited from various subduction events, has been recognized using trace element (e.g. Peccerillo, 1999) and isotopic (e.g. Conticelli *et al.*, 2002) data. Similarly, various crustal, anatectic, end-members have been envisaged for the TMP, all having peraluminous bulk-rock compositions but differing in their Sr and Nd isotopic abundances (Giraud *et al.*, 1986; Pinarelli *et al.*, 1989; Poli, 1992; Dini *et al.*, 2002).

The Monte Capanne pluton

Age

The MC monzogranite (Fig. 2) is the largest intrusion of the TMP (Fig. 1). Published ages range from 7·9 Ma (K–Ar on biotite, Ferrara & Tonarini, 1985) to 6·2 Ma (U–Pb zircon, Juteau *et al.* 1984). As discussed by Dini *et al.* (2002), the most likely emplacement age for the pluton is bracketed between 6·8 and 7·0 Ma mostly based on the Rb–Sr method (Ferrara & Tonarini, 1985; Innocenti *et al.*, 1992). Initial Sr isotopic ratios have, therefore, been calculated at 6·9 Ma (see Table 3). The MC pluton was preceded by the intrusion of a stack of granite porphyries between 8 and 7·4 Ma (Dini *et al.*, 2002) that were emplaced at shallower levels as a series of individual laccoliths (Rocchi *et al.*, 2002). These mostly occur in Central Elba and north of the MC pluton (near Marciana Marina, Fig. 2).

Country rocks

The MC pluton intrudes ophiolitic and sedimentary rocks (161–185 Ma; Ferrara & Tonarini, 1985) belonging to the Ligurian Nappes of the Northern Apennines (Fig. 2), as well as the porphyry laccoliths. The ophiolitic complex (Fig. 2) (Complex IV; Trevisan, 1951) comprises serpentinites, gabbros, pillow lavas and a pelagic sedimentary cover, and is mostly found in central and western Elba (Trevisan & Marinelli, 1967). The intrusion of the pluton locally created a metamorphic aureole in the high hornblende hornfels facies (Bussy, 1990*a*). Angular hornfels xenoliths occur occasionally at the margins of the pluton. These have sharp contacts with the host monzogranite and display no evidence of assimilation.

The main monzogranitic facies

The bulk of the intrusion consists of a monzogranite [Main Facies (MF), Poli *et al.*, 1989]. The texture is hypidiomorphic granular, sometimes strongly porphyritic with K-feldspar megacrysts (Kfm) up to 15 cm long (Fig. 3a) and abundant plagioclase phenocrysts. The mineralogy chiefly consists of plagioclase (28–45%), microperthitic K-feldspar (22–25%), quartz (24–27%) and biotite (<10%). Accessory minerals are apatite, zircon, allanite and monazite. Secondary minerals are chlorite, calcite and muscovite. Based on petrographic and field observations, the MC pluton has been divided into three facies (Sant' Andrea, San Piero and San Francesco facies; Dini *et al.*, 2002), (Fig. 2). The Sant' Andrea facies is characterized by abundant Kfm and large, sometimes composite, MME (Fig. 3b), whereas the San Piero facies exhibits scarce megacrysts (Fig. 3a) and MME. The San Francesco facies can be considered as a transition zone. However, the abundance of zoned plagioclase phenocrysts in both enclave and host (Gagnevin *et al.*, 2004) and reaction micro-textures between accessory minerals in the monzogranite (Dini *et al.*, 2004) indicate that the three facies suffered pervasive hybridization. Overall, the monzogranite has limited major and trace chemical variations (66–70% SiO_2, 1–1·8% MgO) and isotopic variations ($^{87}Sr/^{86}Sr_{(i)} = 0{\cdot}7145$–$0{\cdot}7172$; $^{143}Nd/^{144}Nd_{(i)} = 0{\cdot}51211$–$0{\cdot}51221$) (Poli *et al.*, 1989; Dini *et al.*, 2002; Gagnevin *et al.*, 2004). There is a continuous chemical gradation from the Sant' Andrea facies (more silicic) to the San Piero facies (less silicic) (Dini *et al.*, 2004), despite a reverse gradation in the field for the abundance of MME and Kfm. Despite this chemical zonation, the three facies have similar Sr and Nd isotopic composition, although a trend towards low Nd and high Sr isotopic ratios is interpreted to reflect crustal assimilation (Gagnevin *et al.*, 2004).

Mafic microgranular enclaves

The widespread abundance of granodioritic to monzogranitic MME (from a few centimetres up to 1–2 m across) (Fig. 3b) is a characteristic feature of the MC pluton. Their shape, chemical composition, mineralogy and texture undoubtedly support a magmatic origin as a result of interactions between acid and basic magmas (Poli *et al.*, 1989; Poli, 1992), as demonstrated in other plutons (e.g. Vernon, 1984, 1990; Barbarin, 1990; Didier & Barbarin, 1991).

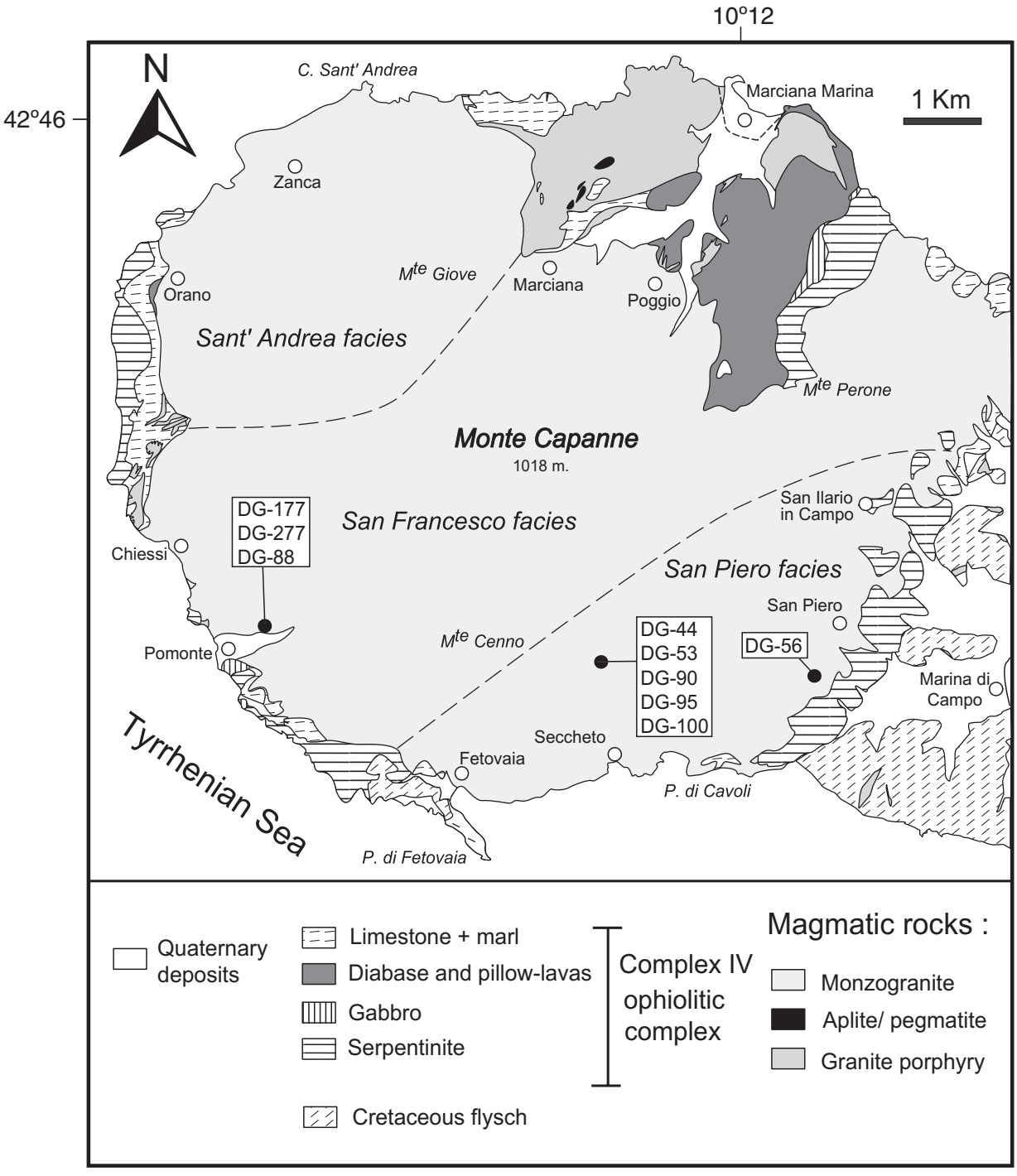

Fig. 2. Geological map of the western part of Elba Island (after Trevisan & Marinelli, 1967) showing the Monte Capanne pluton and the surrounding geology. ○, place names; ●, sample localities with sample numbers of analysed K-feldspar megacrysts; long-dashed lines indicate subdivisions of the pluton into Sant' Andrea, San Francesco and San Piero facies (Dini *et al.*, 2002); short-dashed line shows outline of the town of Marciana Marina.

MME have been investigated in detail by Gagnevin *et al.* (2004). Their mineral content is the same as that of the monzogranite; however, they contain a higher proportion of biotite and abundant acicular apatite needles. Phenocrysts mostly consist of plagioclase and quartz. They commonly exhibit disequilibrium textures (rim of biotite in quartz ocelli, patchy zoning, dissolution surfaces and resorbed An-rich cores in plagioclase), which

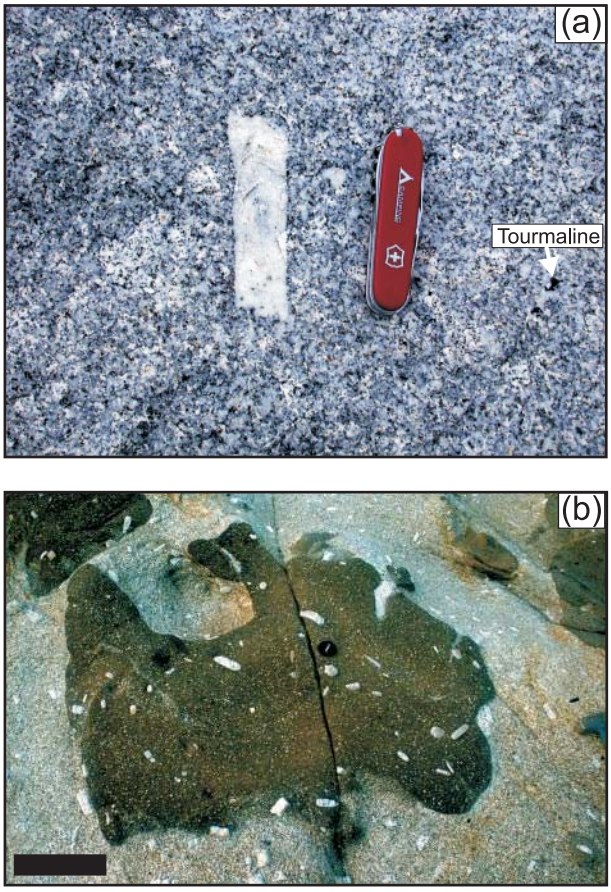

Fig. 3. Field photographs. (a) San Piero facies at Bontempelli Quarry showing a subhedral K-feldspar megacryst (Kfm) and typical tourmaline clots. Penknife measures 9 cm. (b) Large mafic microgranular enclave (MME) in the Sant' Andrea facies of the Monte Capanne monzogranite at Capo Sant' Andrea (Fig. 2). (Note the abundance of megacrysts both within and outside the enclave.) Scale bar represents 20 cm.

emphasize the importance of magma mixing and crystal transfer (Gagnevin *et al.*, 2004). A gabbroic enclave, containing plagioclase and amphibole as main phases, displays low light rare earth elements (LREE) and primitive Sr and Nd isotopic compositions ($^{87}Sr/^{86}Sr_{(i)}$ = 0·7092 and $^{143}Nd/^{144}Nd_{(i)}$ = 0·51239), similar to high-K calc-alkaline volcanic rocks from Capraia (Fig. 1). Apart from this enclave, MME have distinctive major elements (high CaO, MgO), trace element (high Ba, Sr, REE) and isotopic ($^{87}Sr/^{86}Sr_{(i)}$ = 0·7137–0·7159; $^{143}Nd/^{144}Nd_{(i)}$ = 0·51205–0·51223) compositions (although overlapping with the monzogranite) supporting the magma mixing hypothesis. The chemical heterogeneity of the MME in the MC pluton is largely inherited from crystal exchange between basic and acid melt components, further complicated by diffusional exchange with the host monzogranite. Although most MME have lower $^{87}Sr/^{86}Sr_{(i)}$ (0·7136–0·7145) than the monzogranite, some MME have higher $^{87}Sr/^{86}Sr_{(i)}$ (0·7148–0·7159) coupled with lower Nd isotopic ratios ($^{143}Nd/^{144}Nd_{(i)}$ = 0·51205–0·51125), which suggest that the mafic magma may have also experienced crustal contamination (Gagnevin *et al.*, 2004).

Metasedimentary xenoliths

Metasedimentary xenoliths are randomly distributed in the MC pluton. Their concentration can reach up to 15 per m^2 (average size <1 cm^2), although they represent less than 0·1% of the volume. They mostly consist of surmicaceous enclaves (Didier, 1973) and gneissic fragments. Textures are granoblastic to lepidoblastic. Biotite, together with plagioclase and subordinate quartz, defines the main foliation, with occasional leucosomes made of quartz and plagioclase. Surmicaceous enclaves are made of biotite (>40%), plagioclase and various aluminous minerals (corundum, cordierite, hercynite, andalusite and sillimanite). Gagnevin *et al.* (2004) suggested that these xenoliths represent pelitic fragments partially digested during magma storage in the Tuscan basement. This hypothesis is further discussed below.

ANALYTICAL METHODS

Samples

The Kfm investigated in this study were collected from three quarries [San Piero (DG-56), Seccheto (DG-44, -53, -90, -95, -100) and Pomonte (DG-88, -177, -277) quarries (Fig. 2)] where fresh samples could be collected. As a result, we lack suitable megacrysts from the northwestern side of the pluton, where the exposures are abundant, but often weathered and altered. The average number of megacrysts in San Piero (5 per m^2) is lower that in Seccheto (*c.* 20 per m^2) and Pomonte (*c.* 15 per m^2). Only megacrysts with minimal alteration and displaying at least one resorption surface (Fig. 4) have been investigated in this study. These represent only about 5–10% of the Kfm population in the MC monzogranite. Two of the investigated megacrysts (DG-44 and DG-90) have a plagioclase mantle, which is prominent (*c.* 7 mm thick) in megacryst DG-44 (Fig. 5a), but much thinner in megacryst DG-90 (<1 mm thick). Analyses of selected megacrysts were carried out on polished surfaces cut in a known orientation; that is, perpendicular to the {010} Carlsbad twin plane. For megacrysts DG-177 and DG-100, two sections at right angles to one another [i.e. $DG\text{-}177_{(1)}$ and $DG\text{-}100_{(1)}$ parallel to {001} and $DG\text{-}177_{(2)}$ and $DG\text{-}100_{(2)}$ parallel to {100}] were analysed.

Electron microprobe

Major and minor element (Ba) analyses of Kfm and their plagioclase and biotites inclusions were performed

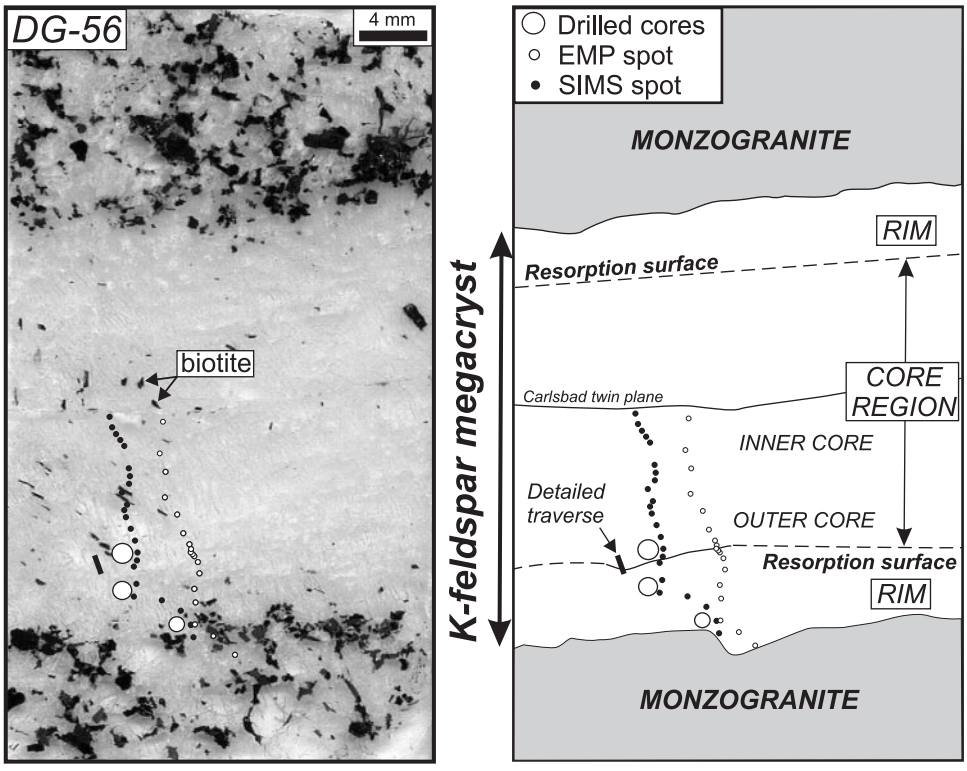

Fig. 4. Photograph and sketch of the analysed thin-section from sample DG-56 (San Piero) showing the host monzogranite facies (top and bottom) and the Kfm, from which electron microprobe (open small spots) and ion microprobe data (filled small spots) were obtained. Large open spots show the position and diameter of the 200 μm long, microdrilled cores analysed for Sr isotopes. Black rectangle shows the location of the detailed ion microprobe traverse (Figs 10 and 14). The sketch shows both edges of the megacryst, the Carlsbad twin plane and the positions of the resorption surfaces. 'Rim' corresponds to the area rimward, and 'core region' to the area coreward, of the resorption surface. The distinction between inner and outer core is only defined based on trace element variations within the core region (see text). Images of the other Kfm analysed in this study are shown in Electronic Appendices 1–3 at http://www.petrology.oupjournals.org.

by electron microprobe analysis (EMPA) at the Department of Earth-Sciences, University of Bristol, using a JEOL JXA 8600 electron microprobe fitted with four wavelength-dispersive spectrometers. Analyses were carried out at 20 kV, using a beam current of 15 nA and a 5 μm spot size. Under these operating conditions and 45 s on the Ba peak, the detection limit for Ba is 750 ppm with a precision of *c.* 15% (relative). International standards were analysed prior to each run to check the accuracy of the analyses.

Ion microprobe

Trace elements in Kfm were analysed by secondary ion mass spectrometry (SIMS), using a CAMECA ims-4f ion microprobe at the Department of Geology and Geophysics, University of Edinburgh. SIMS analyses were carried out on the same sections previously analysed by EMPA, except for megacryst DG-44, for which a separate section parallel was used. Samples were polished, cleaned and coated with gold prior to analysis. A beam of primary negative ions (O^-) was used to create positive secondary ions from a duoplasmatron source (Hinton, 1995). The primary beam (6–7 nA) was focused on a *c.* 20 μm diameter spot at the sample surface, and ions were measured at masses 7 (Li), 11 (B), 26 (Mg), 30 (Si), 31 (P), 42 (Ca), 39 (K), 52 (Cr), 85 (Rb), 88 (Sr), 133 (Cs), 138 (Ba). An energy filtering technique (ions recorded at 75 ± 20 eV) was used to reduce molecular ion interferences to negligible values. Si content, which was determined using the electron microprobe, was used as internal standard. The counting time for each element was 2 s (Si, Li, Rb, Sr), 5 s (B, Ca), 7 s (P) or 10 s (Cs, Cr, Mg). The matrix effect (i.e. ion yields relative to a standard) was evaluated using the glass standard NIST-610, which was analysed prior to each analytical session. The precision of the spot analyses can be gauged from counting statistics and is better than 1% for Li, Rb and Sr (at 500 ppm), better than 2% for Mg and Ca (at 500 ppm) and 5% for P (at 200 ppm). The precision for B is 4% (at 0·5 ppm), about 6% for Cs (at 3 ppm) and *c.* 25% for Cr (at 0·2 ppm). The accuracy of the analysis was evaluated by repeatedly analysing feldspar [Lake County plagioclase, SHF1 (mol % Or = 30; Irving & Frey, 1984)]

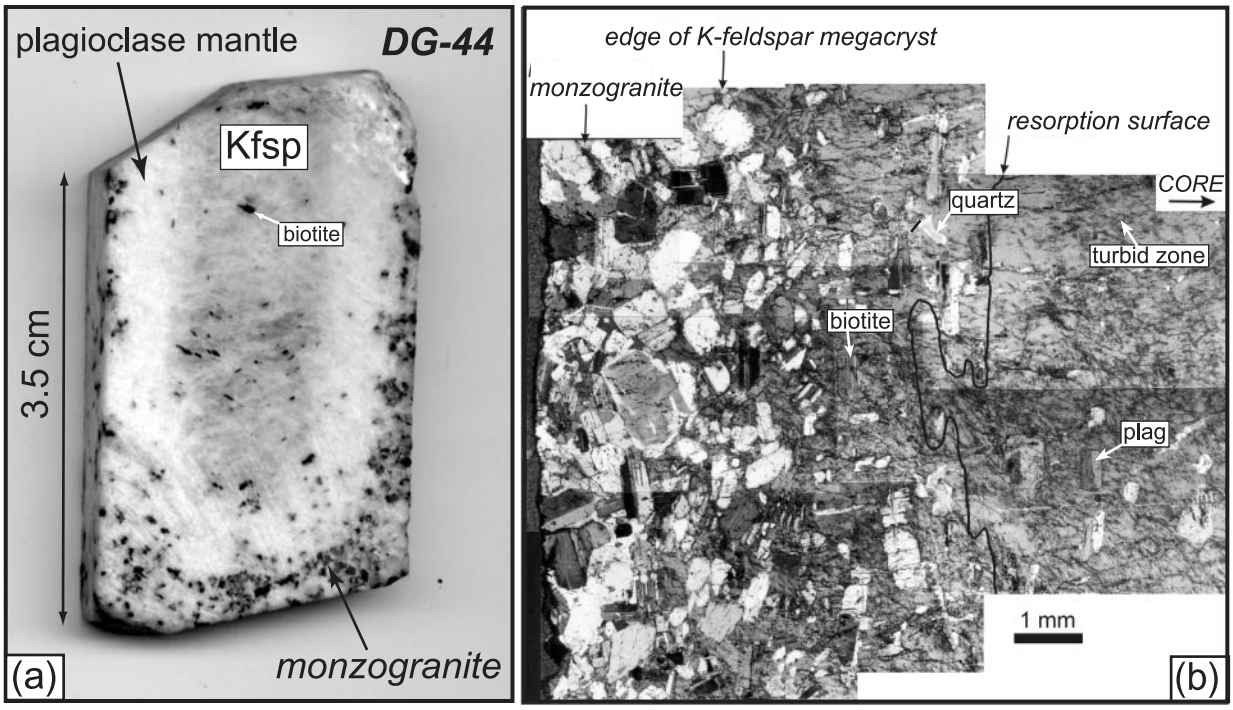

Fig. 5. (a) Photograph of a slice through K-feldspar megacryst DG-44 from the monzogranite north of Seccheto showing a plagioclase mantle (rapakivi texture). These are more common in MME from the MC pluton. (b) Composite photomicrograph showing part of a zoned K-feldspar megacryst (sample 10/96-15, San Piero; Daly & Poli, 1999) in contact with the host monzogranite (left). (Note the irregular shape of the resorption surface as well as abundant plagioclase inclusions rimward of it.)

and borosilicate glass standards (Corning Glasses) as unknowns. The accuracy is better than 10% for B, Li, Mg, K, Ca, Rb, Sr, Ba and Cs, and better than 20% for P and Cr. Detection limits are 0·5 ppm for Cr, 0·3 ppm for Ca, and <0·1 ppm for all the other elements.

Sr isotope analysis

Kfm were cored using a diamond-coated microscope-mounted microdrill at the Department of Earth Sciences, University of Leeds. Microdrilling was carried out on section chips (150–250 μm thick) previously used for electron microprobe and SIMS analyses. Kfm were preferentially drilled in pristine areas of the megacrysts to minimize the effects of secondary alteration (e.g. sericite veins, patch perthites, etc.). Therefore, the density of microdrilled cores as well as their size was limited. Drill core size ranges from 200 μm to >1 mm, corresponding to sample weights <0·15 mg. When extracted, the K-feldspar cores were further inspected under a binocular microscope. Instead of collecting a slurry made of crystal powder and water (e.g. Knesel *et al.*, 1999; Tepley *et al.*, 1999), this technique allows the sample to be entirely preserved, thus allowing careful inspection and selection of parts of the samples free of inclusions (mostly biotite and plagioclase). The selected cores were cleaned in an ultrasonic bath using alternating cycles of acetone and water.

Microsamples were dissolved in a $HF–HNO_3$ mixture and spiked using a mixed ^{87}Rb–^{84}Sr spike. Chemical separation on miniaturized columns was performed using standard ion-exchange resins for Rb and Sr separations. Total procedural blanks for the microsample chemistry varied between 0·13–0·30 ng for Sr and <0·08 ng for Rb. Analyses were performed on a single-collector Micromass 30 thermal ionization mass spectrometer at the Department of Geology, University College Dublin. For Sr analyses, samples were loaded on single Re filaments using a tantalum emitter in order to improve the ionization efficiency. Samples were loaded on Ta filaments for Rb analyses. During the course of the analyses, NIST SRM 987 standard solution (*c.* 20 ng loaded after the whole separation procedures) gave a mean $^{87}Sr/^{86}Sr$ value of $0{\cdot}710265 \pm 31$ (2σ, $n = 9$). Considering the total amount of Sr in the microsamples (Table 3), a fixed blank correction has been applied, taking a maximum blank of 0·3 ng and a blank isotopic ratio of $^{87}Sr/^{86}Sr = 0{\cdot}710$, which we consider results in a maximum blank correction. The results show that the 2σ error (including the blank correction and multiple standard runs) is below 200 ppm for most samples (>15 ng Sr) and does not

impinge on the interpretation of the data, with the possible exception of smaller samples (<10 ng; 2σ uncertainty of 250–600 ppm; Table 3). Uncertainty in the age of the intrusion (6·9 ± 0·1 Ma; Dini *et al.*, 2002) is within the 2σ uncertainty, which may not be the case when older intrusions are investigated using similar microsampling techniques (e.g. Cox *et al.*, 1996; Waight *et al.*, 2000*a*, 2000*b*).

Comparisons between the different techniques

We note that (1) the Ba concentration obtained by SIMS and EMPA (see Fig. 9a–c) and (2) the Rb/Sr ratio obtained by isotope dilution TIMS and SIMS analyses (Table 3; Electronic Appendix 5), are in good agreement. Some discrepancies arise from the different sampling scale (i.e. *c.* 20 μm for SIMS spots and >200 μm for TIMS analyses), but in general, the different methods agree very well.

Images of the investigated megacrysts with the location of the electron and ion microprobe spots as well as the position of the microdrilled cores are available as electronic supplements (Electronic Appendices 1–3) at http://www.petrology.oupjournals.org. One example (e.g. megacryst DG-56) is displayed in Fig. 4. The occurrence of resorption surfaces (Fig. 4) as well as the distinction between different parts of the megacryst (inner and outer core region, rim etc., Fig. 4) is discussed in detail below.

K-FELDSPAR PETROGRAPHY

Inclusions

Kfm grains contain numerous inclusions of biotite, plagioclase and quartz, which are more abundant towards the rim (Fig. 5b). The plagioclase inclusions (*c.* 0·2–1·5 mm) are often smaller in size than the crystals observed in the host (>1 mm). Subhedral inclusions tend to be oriented parallel to {010}, {001} and {110} of the host K-feldspar (Franzini & Leoni, 1974), especially in zones close to major resorption surfaces (see below). The cores of the plagioclase inclusions are relatively homogeneous (31 < mol % An < 38, Table 1, Fig. 6), and no systematic spatial variation in plagioclase composition was observed (Franzini *et al.*, 1974). The rims are generally more sodic (10 < mol % An < 26; Fig. 6). Rare An-rich plagioclase inclusions (47 < mol % An < 71; Fig. 6) are similar to An-rich plagioclase observed in MME and the host monzogranite (Gagnevin *et al.*, 2004). Quartz inclusions are typically organized elongated xenomorphic septa, often occurring in optical continuity with the sodic rim of the plagioclase inclusions.

Biotite inclusions are euhedral to subhedral (Figs 4 and 5a) and contain abundant concentric inclusions of apatite and zircon. Together with plagioclase, biotite crystals define trails of inclusions. Biotite inclusions display a limited range of composition ($0{\cdot}477 < X_{Fe} < 0{\cdot}546$; $3{\cdot}2\% < TiO_2 < 4\%$), which is within the range of biotite found in the monzogranite ($0{\cdot}387 < X_{Fe} < 0{\cdot}546$) and MME ($0{\cdot}242 < X_{Fe} < 0{\cdot}543$) (Gagnevin *et al.*, 2004).

Perthites

Two types of perthitic feldspar were observed by scanning electron microscopy (SEM). The first type corresponds to microperthite lamellae (between 1 and 5 μm wide; Fig. 7a), and the second type is coarse patch perthite (between 10 and 50 μm wide; Fig. 7a). The presence of turbid areas within the K-feldspar megacrysts (Fig. 5b) corresponds to a high density of patch perthite coupled with the abundance of micropores (e.g. Lee *et al.*, 1995). Patch perthites formed during coarsening and exsolution of early-formed microperthites, as clearly evidenced in Fig. 7a and b, and observed by Lee *et al.* (1995). Patch perthites are also more sodic than microperthitic K-feldspar (Fig. 6). Patch perthites may be surrounded by non-perthitic K-feldspar (whiter zone surrounding the perthites; Fig. 7a), indicating that Na migrated away from the microperthite to form patch perthites. Whereas the formation of microperthites is related to early stage of K-feldspar exsolution at temperatures below 600°C (Lee *et al.*, 1995; Smith & Brown, 1998), coarse patch perthites are attributed to late deuteric fluid circulation along lamellae at temperatures below 400°C (e.g. Lee *et al.*, 1995).

Resorption surfaces

Detailed SEM observations reveal the occurrence of prominent xenomorphic resorption surfaces (Daly & Poli, 1999; Figs 5b and 6b), which coincide with an increased abundance of mineral inclusions in the succeeding K-feldspar (Fig. 5b). Identifying the resorption surfaces precisely is possible only using backscattered electron (BSE) images (Fig. 7b). Resorption surfaces have an irregular shape, often displaying complex 'indentations' (Fig. 5b). On a small-scale (i.e. under BSE), the transition across resorption surfaces is sharp and easily recognized (Fig. 7b). The K-feldspar rimward of the resorption surface appears brighter (Fig. 7b) as a result of higher mean atomic number, largely owing to a higher Ba content (see below). The transition from lower to higher atomic number (i.e. rimward of the resorption surface) in the K-feldspar often occurs through an intermediate brighter zone (10–50 μm wide) where no microperthites are observed (Fig. 7b). K-feldspar megacrysts rimward of the resorption surfaces often consists of a 'matrix' of high-Ba K-feldspar and numerous 'enclaves' of low-Ba K-feldspar, reminiscent

Table 1: Selected electron microprobe analyses of K-feldspar and plagioclase in the Monte Capanne pluton

	K-feldspar megacrysts								
Sample:	DG-90	DG-90	DG-90	DG-44	DG-44	DG-44	DG-56	DG-56	DG-56
Location:	Seccheto	Seccheto	Seccheto	Seccheto	Seccheto	Seccheto	San Piero	San Piero	San Piero
Position:	core region	rimward of r.z.	outer rim	core region	rimward of r.z.	outer rim	core region	rimward of r.z.	outer rim
SiO_2	65·13	64·32	65·21	64·80	64·76	64·17	64·79	64·8	64·71
Al_2O_3	19·40	19·39	18·89	19·15	19·09	18·69	19·40	19·4	18·56
CaO	0·11	0·10	0·06	0·17	0·13	0·01	0·12	0·1	0·03
Na_2O	2·68	2·83	1·49	2·86	2·68	0·85	2·16	2·3	0·91
K_2O	13·38	12·65	14·95	12·52	12·61	15·61	13·65	13·1	15·86
BaO	0·10	1·09	d.l.	0·26	1·21	d.l.	0·30	1·0	0·14
Sum	100·70	100·39	100·64	99·76	100·47	99·32	100·46	100·7	100·26
An	0·5	0·5	0·3	0·8	0·6	0·1	0·6	0·6	0·2
Ab	23·2	25·3	13·1	25·5	24·3	7·6	19·2	21·3	8·0
Or	76·2	74·2	86·6	73·6	75·1	92·3	80·2	78·2	91·8

	Plagioclase inclusions					Plagioclase in rapakivi mantle		
Sample:	DG-100	DG-177	DG-90	DG-90	DG-56	DG-44	DG-44	DG-90
Location:	core, res.	core	core	rim	core	core	core	core
SiO_2	49·24	59·19	59·42	65·30	58·61	59·33	62·25	61·25
Al_2O_3	32·96	25·43	25·78	21·77	26·68	25·33	23·35	24·27
CaO	14·94	6·59	6·83	1·81	7·40	6·77	4·49	5·13
Na_2O	3·22	7·75	7·51	10·10	7·00	7·76	8·93	8·63
K_2O	0·08	0·36	0·28	0·91	0·30	0·34	0·41	0·00
BaO	d.l.	d.l.	d.l.	d.l.	d.l.	d.l.	d.l.	d.l.
Sum	100·48	99·35	99·82	99·89	99·98	99·54	99·42	99·65
An	71·6	31·3	32·9	8·5	36·3	31·9	21·2	24·3
Ab	27·9	66·7	65·5	86·4	62·0	66·2	76·5	73·9
Or	0·5	2·0	1·6	5·1	1·7	1·9	2·3	1·8

r.z., resorption zone; res., resorbed; d.l., below detection limit. The full dataset is available in Electronic Appendix 4 at http://www.petrology.oupjournals.org.

of and sometimes connected to the core, giving a patchy texture. In the investigated samples, we detected up to three resorption surfaces (in DG-88). Most of zoned megacrysts have either one or two resorption surfaces.

Typically, plagioclase inclusions are more abundant rimward of the resorption surfaces (Fig. 5b). Although not systematic, acicular apatite needles parallel to the resorption surfaces also can occur. These either are found 'sticking' on the resorption surface or can be observed for up to 1–2 mm rimwards. The influence of apatite growth on the phosphorus budget of the Kfm is discussed below.

For orientation purposes, especially when discussing chemical and isotopic zoning (see below), we define the K-feldspar rimward of the resorption surface to be the 'rim' (Fig. 4), whereas the 'core region' comprises the K-feldspar coreward of the resorption surface (Fig. 4).

Plagioclase mantling

K-feldspars with a mantle of plagioclase (i.e. rapakivi texture) are abundant within the MC pluton (Fig. 5a), and were described in detail by Bussy (1990*b*). Plagioclase mantles are made of coexisting andesine ($31 < \text{mol \% An} < 36$) and oligoclase ($10 < \text{mol \% An} < 20$) crystals (Table 1), with little interstitial quartz and K-feldspar.

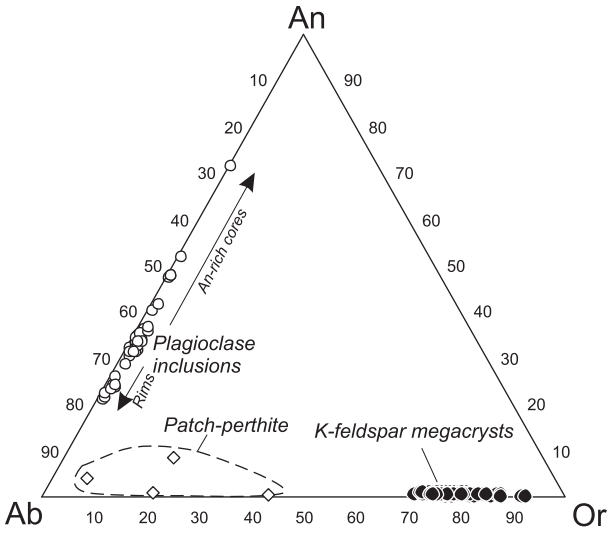

Fig. 6. Major element compositions (determined by electron microprobe; see Electronic Appendix 4 at http://www.petrology.oupjournals.org) of K-feldspar megacrysts, patch perthites and plagioclase inclusions represented in terms of albite (Ab), anorthite (An) and orthoclase (Or) end-members. The wide compositional range of plagioclase inclusions is noteworthy, although the cores mostly cluster at $30 < \text{mol \% An} < 40$, whereas the rims are more sodic. A noteworthy feature is the occurrence of An-rich inclusions, similar to resorbed plagioclase crystals in both MME and the monzogranite. These are interpreted to result from early magma mixing between crustal and mafic, mantle-derived magmas (Gagnevin *et al.*, 2004).

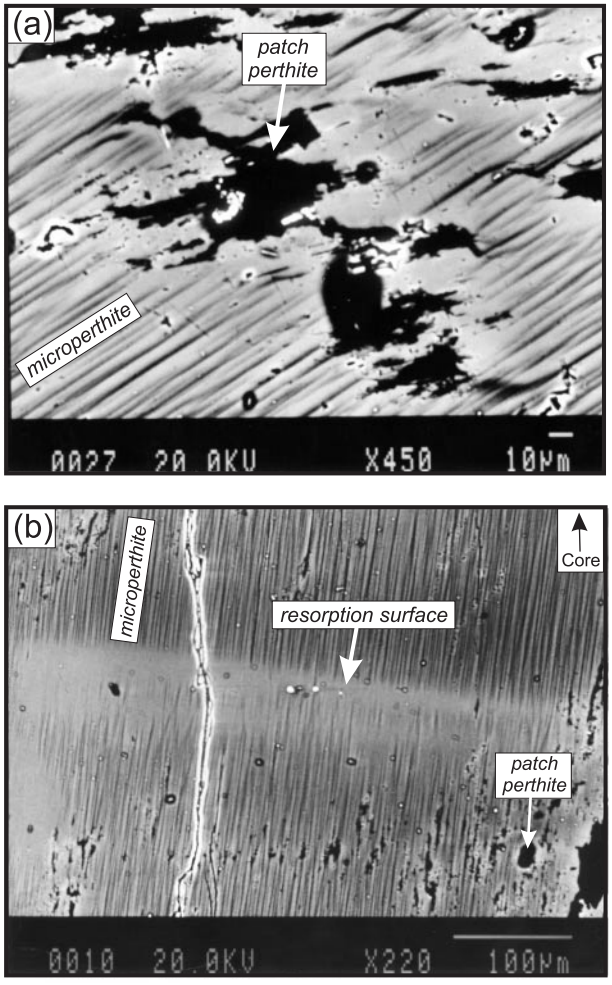

Fig. 7. Backscattered-electron (BSE) images of Kfm in which higher brightness (as a result of higher average atomic number) is mainly controlled by Ba content. (a) Patch perthite (black areas) cutting across microperthite lamellae. (b) Image of a major resorption surface (from Gagnevin *et al.*, 2004) parallel to {100}. The narrow zone (10–50 µm wide) lacking microperthite rimward of the resorption surface should be noted.

CHEMICAL ZONING

Major and minor elements

Detailed core to rim traverses of zoned megacrysts previously investigated by SEM were obtained by electron microprobe. We show eight megacryst traverses in Fig. 8, where the mol % Or and BaO % are plotted as a function of the distance normalized to the megacryst cores (i.e. rim-to-rim (Fig. 8a) or core-to-rim (Fig. 8b) distance measured relative to the middle point of each traverse). The complete dataset including the major and minor element composition of the eight megacrysts (together with analyses of plagioclase inclusions; Fig. 6) is available in Electronic Appendix 4 at http://www.petrology.oupjournals.org.

Zoned megacrysts are characterized by a sharp increase of BaO (up to 1–1·2 wt %) rimward of the resorption surfaces (Fig. 8a and b, Table 1). The transition from low- to high-Ba K-feldspar is generally sharp (>0·4% BaO; Fig. 8a and b), although, in detail, a gradual increase of Ba is observed over <200 µm of crystal growth [see, for example megacrysts DG-56 (Fig. 8b) and DG-177$_{(2)}$ (Fig. 8a); Electronic Appendix 4]. Kfm grains displaying two (or more) resorption surfaces (DG-53, -88, -95 and -100) have a pronounced patchy texture, resulting in thicker Ba-rich rims (Fig. 8a and b). Strangely, the two resorption surfaces in megacryst DG-53 (Fig. 8a) occur at almost exactly the same distance from the core as the single resorption surfaces in DG-44 and DG-90 (Fig. 8a). In the core region, Ba either displays large oscillations (e.g. DG-44, DG-90) and/or increases towards the rim ('reverse zoning', e.g. DG-53, -88, -100) (Fig. 8a and b). Reverse zoning is more pronounced in megacrysts that display two (or more) resorption surfaces.

The major element composition in the core region of the megacrysts varies between 70 and 82 mol % Or and is generally independent of the Ba zoning (Fig. 8a and b). The rim has a wider range of mol % Or (62–94) than the core and may be correlated with Ba in the outer rim (Ba decreases, mol % Or increases; Fig. 8a and b).

For megacrysts DG-100 and DG-177, electron probe traverses were obtained from two perpendicular surfaces (see above; Fig. 8a and b) in view of the possibility that zoning can be dependent on crystallographic orientation

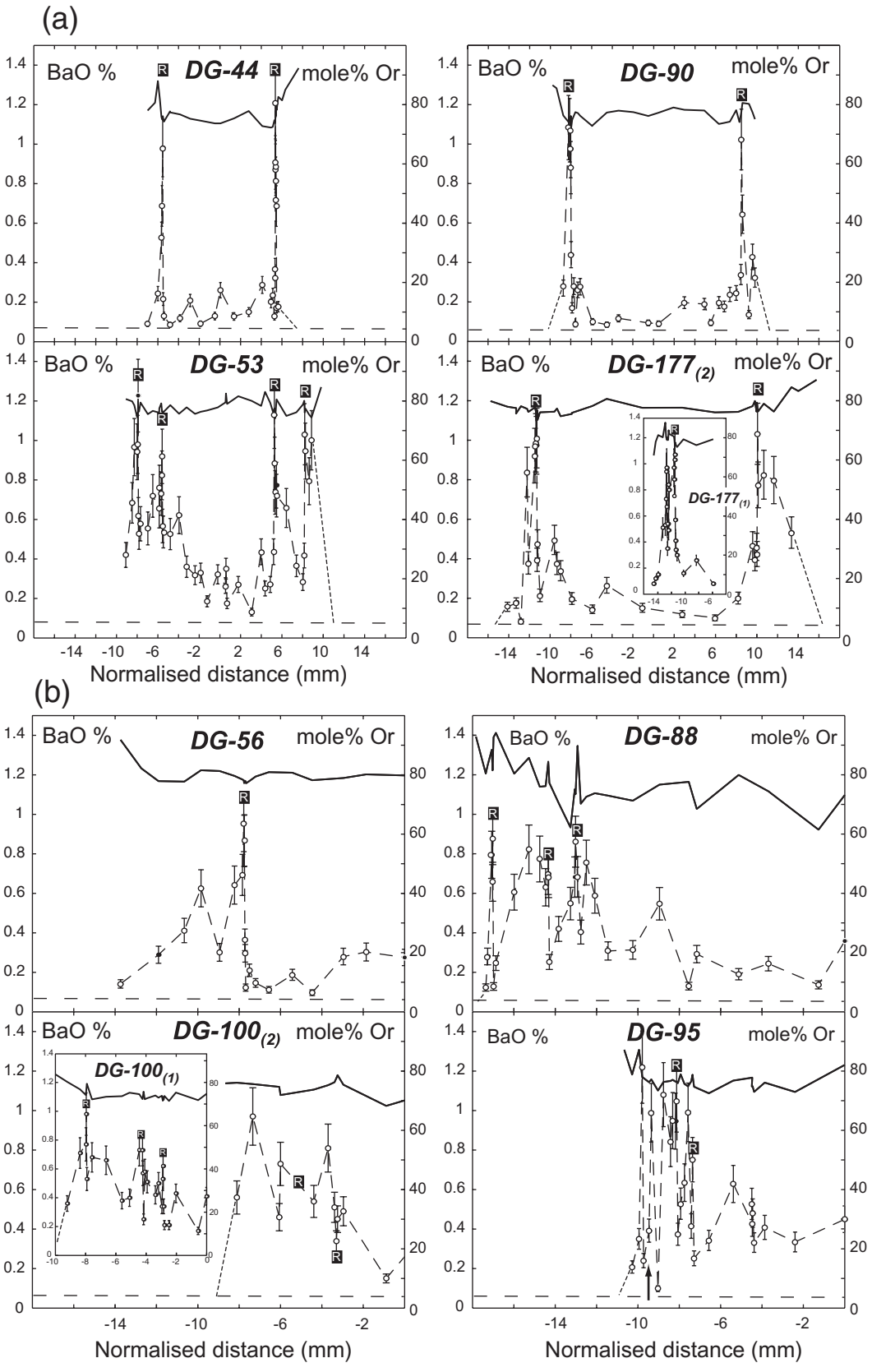

(e.g. Shimizu, 1981; Cox *et al.*, 1996). However, both megacrysts exhibit very similar zoning on the two surfaces analysed. Thus it seems that zoning can be replicated in three dimensions, further strengthening the interpretation of the isotopic and elemental profiles. We note that three resorption surfaces have been detected in DG-$100_{(1)}$, instead of two in DG-$100_{(2)}$ (Fig. 8b).

Trace elements

Trace element zoning was determined by SIMS on K-feldspar megacrysts previously analysed by EMPA. We investigated five megacrysts from the San Piero, Seccheto and Pomonte quarries (Fig. 2). Analyses were carried out from core to rim, with an average of *c.* 200 μm spacing between each analysis (Fig. 4), although larger gaps were sometimes necessary to avoid turbid regions or mineral inclusions. The full dataset of ion microprobe trace element analyses is available in Electronic Appendix 5 at http://www.petrology.oupjournals.org.

Two sets of trace elements have been used: (1) Ba, Rb, Sr, Li and P (for DG-56, DG-90 and DG-$177_{(2)}$) and (2) Ba, Rb, Sr, Li, Mg (for DG-44 and DG-$100_{(2)}$). Cr analyses of DG-44 and DG-$100_{(2)}$ proved to be largely unsuccessful because Cr was close to the detection limit (<0·5 ppm), and was instead replaced by P (Fig. 9a–c). For megacrysts DG-44 and DG-$100_{(2)}$, Ba analyses obtained by EMPA have been used (Fig. 9d and e). These are directly comparable with SIMS data, as shown for the other megacrysts for which Ba analyses were also obtained using both SIMS and EMPA (Fig. 9a–c). Mg profiles are shown for megacrysts DG-44 (Fig. 9d) and DG-$100_{(2)}$ (Fig. 9e). The reader is referred to Electronic Appendix 5 for the Mg (only for DG-56, DG-90 and DG-177), Ca, Cs and B profiles.

In some cases, the inner core (i.e. closer to the core) and the outer core (i.e. closer to the resorption surface) are distinguished on the basis of trace element variations observed in the core region (Fig. 4).

Generally, megacrysts DG-56 (Fig. 9a), DG-90 (Fig. 9b) and DG-$177_{(2)}$ (Fig. 9c) have comparable zoning patterns in the rims, which have high Sr and Ba contents that decrease outwards. Megacryst DG-$100_{(2)}$ strongly differs from the other megacrysts at the core (high Sr, Fig. 9e), whereas megacryst DG-44 differs at the rim (low Sr, Fig. 9d). Despite these differences, the investigated Kfm grains share at least parts of their zoning patterns, which are detailed below.

Effect of alteration

Turbid zones in K-feldspar megacrysts (Fig. 5b) are common and reflect late-stage alteration by meteoric or hydrothermal fluids (Lee *et al.*, 1995). SIMS analyses were targeted away from these zones, although overlaps were sometimes unavoidable. We performed analyses in both pristine and turbid areas of the K-feldspar in close proximity (<50–100 μm), showing that turbid zones are enriched in B (up to 50 ppm, average <4 ppm in pristine areas) and Cs (up to 160 ppm, average <10 ppm in pristine areas) (Table 2; Electronic Appendix 5). Pristine K-feldspar may also be enriched in B and Cs, possibly because of the presence of micro-inclusions of biotite (see Electronic Appendix 5 for ion microprobe analyses of biotite in DG-56) and/or tourmaline. B and Cs may also be trapped in late Ab-rich patch perthites (Mason *et al.*, 1985), or in microscopic fluid inclusions. SIMS analyses that display suspect high Cs and B concentrations (<15% of the data) are reported in the following profiles, but are clearly indicated (grey squares; Fig. 9). In particular, sporadic enrichment of Rb should be interpreted cautiously. It is possible that the migration of Cs, B and Rb was associated with the transport of Na (same valency as Rb and Cs) during the formation of patch perthites.

Megacryst DG-56

In the inner core, the increase of Rb/Sr (from 0·9 to 1·7) is coupled with a decrease of Ba and a four-fold increase of P (Fig. 9a). The transition to the outer core region is characterized by a decrease of Rb/Sr (from 0·7 to 1·5) and P and an increase in Ba (Fig. 9a), whereas an increase of Li occurred earlier (Fig. 9a). Rimward of the resorption surface, the dramatic increase of Ba and decrease of P are noteworthy. P varies rather little in the rim, which contrasts with greater variations in Ba, Sr and Li (Fig. 9a).

A detailed traverse (Fig. 4) was obtained across the resorption surface in megacryst DG-56 (20 μm between each point, Fig. 10) to investigate possible diffusion across zones of contrasted composition. Rb, Sr and Ba, which have contrasting partition coefficients (Icenhower & London, 1996), were analysed, as well as Cs (Electronic Appendix 5), as this element is particularly sensitive to alteration (see above). The resulting profiles illustrate marked decoupling between Rb, Sr and Ba in the outer core (Fig. 10). Sr displays a pronounced increase over 2 mm (from 5·8 mm to 4·8 mm) towards the rim (Fig. 10), followed by a sharp decrease over 0·2 mm (hereafter

Fig. 8. Mol % Or (continuous line) and BaO % content (dashed line) across eight K-feldspar megacrysts (electron microprobe analyses). (a) Rim to rim profiles; (b) core to rim profiles; (R) denotes the position of resorption surface. The horizontal dashed line is the detection limit for Ba (750 ppm). The 'normalized distance (mm)' is the distance measured relative to the mid-point of each traverse. For megacrysts DG-100 and DG-177 two traverses were obtained at right at angles to one other (i.e. DG-$100_{(1)}$ and DG-$177_{(1)}$ parallel to {001}; DG-$100_{(2)}$ and DG-$177_{(2)}$ parallel to {100}). The two traverses are similar. The distinctive increase of BaO% at the resorption surfaces should be noted. The black arrow in megacryst DG-95 illustrates the patchy texture rimward of the resorption surfaces. (See text for details.)

called 'the 0·2 mm zone') before the resorption surface (Fig. 10). Ba is constant over the same outer core interval and increases steadily in the 0·2 mm zone approaching the resorption surface (Fig. 10). Rb displays an overall decrease in concentration with superimposed small-wavelength variations that also become more pronounced rimwards (Fig. 10).

Megacryst DG-90

Unlike most megacrysts, the inner core of megacryst DG-90 displays little variation in Ba (1221 ± 71 ppm) and Sr (278 ± 13 ppm) (Fig. 9b). Rb, Li and possibly P have a 'wavy' pattern (Fig. 9b), such as those described by Halama *et al.* (2002). The outer core of DG-90 is very similar to DG-56 (Fig. 9b), but the initial increase of Ba in the outer core (from 2·7 mm, Fig. 9b) is followed by a distinctive decrease mirrored by an increase of P (Fig. 9b). A rimward decrease of Ba, Sr and Li and an increase in Rb is observed after the resorption surface (Fig. 9b).

Megacrysts DG-177$_{(2)}$ and DG-277

The inner core of megacryst DG-177$_{(2)}$ exhibits large oscillations in Ba, Rb, Sr, P and Li (Fig. 9c). The Rb/Sr ratio decreases in the outer core (from 8·5 mm to 4·8 mm, Fig. 9c), similar to the pattern seen in DG-90 (Fig. 9b) and DG-56 (Fig. 9a). In the outer core, the gradual decrease of the P is noteworthy, and over the same interval, the increase of Ba is followed by a decrease towards the resorption surface (Fig. 9c), similar to the pattern in megacryst DG-90 (Fig. 9b).

The rim of megacryst DG-177$_{(2)}$ is characterized by a decrease of Sr and Ba towards the outer rim (down to 162 ppm Ba and 148 ppm Sr, Fig. 9c). The range of the Rb/Sr ratio in the rim of DG-177$_{(2)}$ (Rb/Sr = 0·7–2·7) spans almost the entire range of variation in the other megacrysts (Fig. 9c).

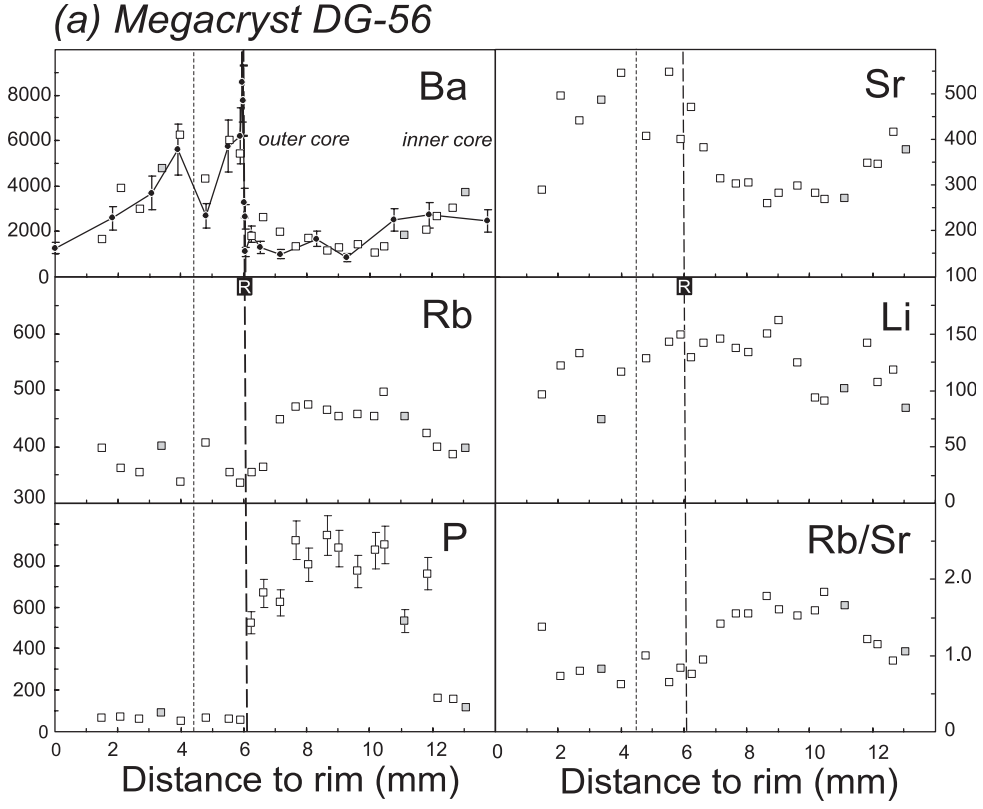

Fig. 9. SIMS profiles for selected trace elements in megacrysts: (a) DG-56; (b) DG-90; (c) DG-177$_{(2)}$; (d) DG-44; (e) DG-100$_{(2)}$ (see Fig. 2 for sample localities). As a proxy for alteration (i.e. in turbid zones), analyses with high B and Cs contents are shown as grey filled squares (see text). The EMPA and SIMS Ba profiles are similar for megacrysts DG-56, DG-90 and DG-177$_{(2)}$. Therefore, Ba data obtained by EMPA are used for megacrysts DG-44 and DG-100$_{(2)}$ for which SIMS analyses are not available. P zoning is shown in (a), (b) and (c), and Mg zoning is shown in (d) and (e) (see text for explanation). The bold dashed line (labelled R) represents the resorption surface. The fine dashed line in (a) marks a change in composition on both the SIMS and EMPA profiles (see text), which may reflect the transfer of the megacryst out of the MME, in which resorption had previously occurred. Error bars are shown for Ba EMPA data and P by SIMS. Otherwise errors are smaller than the symbol size. Ca, Mg, Cs and B for DG-56, DG-90 and DG-177$_{(2)}$, and Ca, Cs and B for DG-44 and DG-100$_{(2)}$ are reported in Electronic Appendix 5 at http://www.petrology.oupjournals.org.

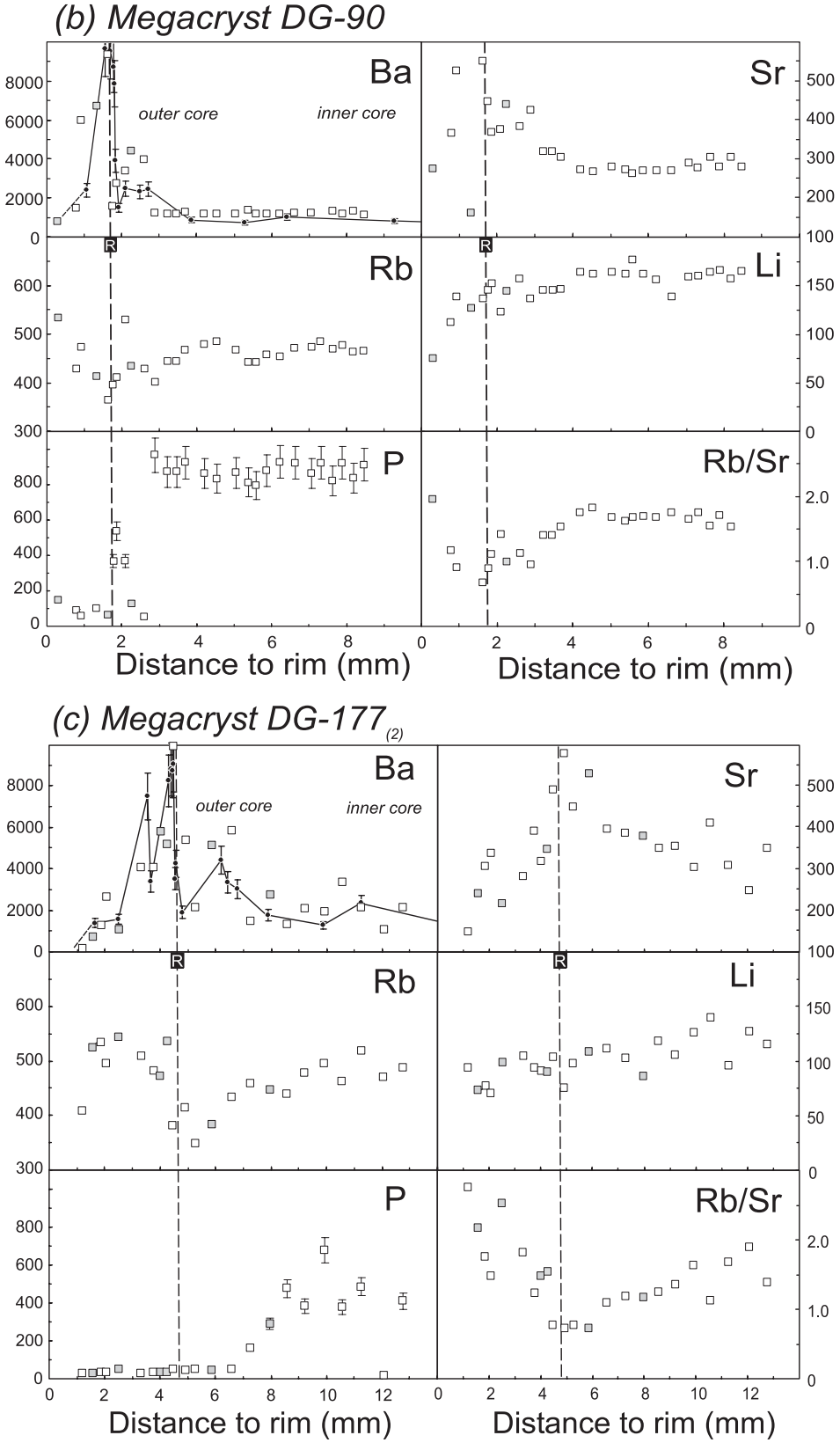

Fig. 9. Continued.

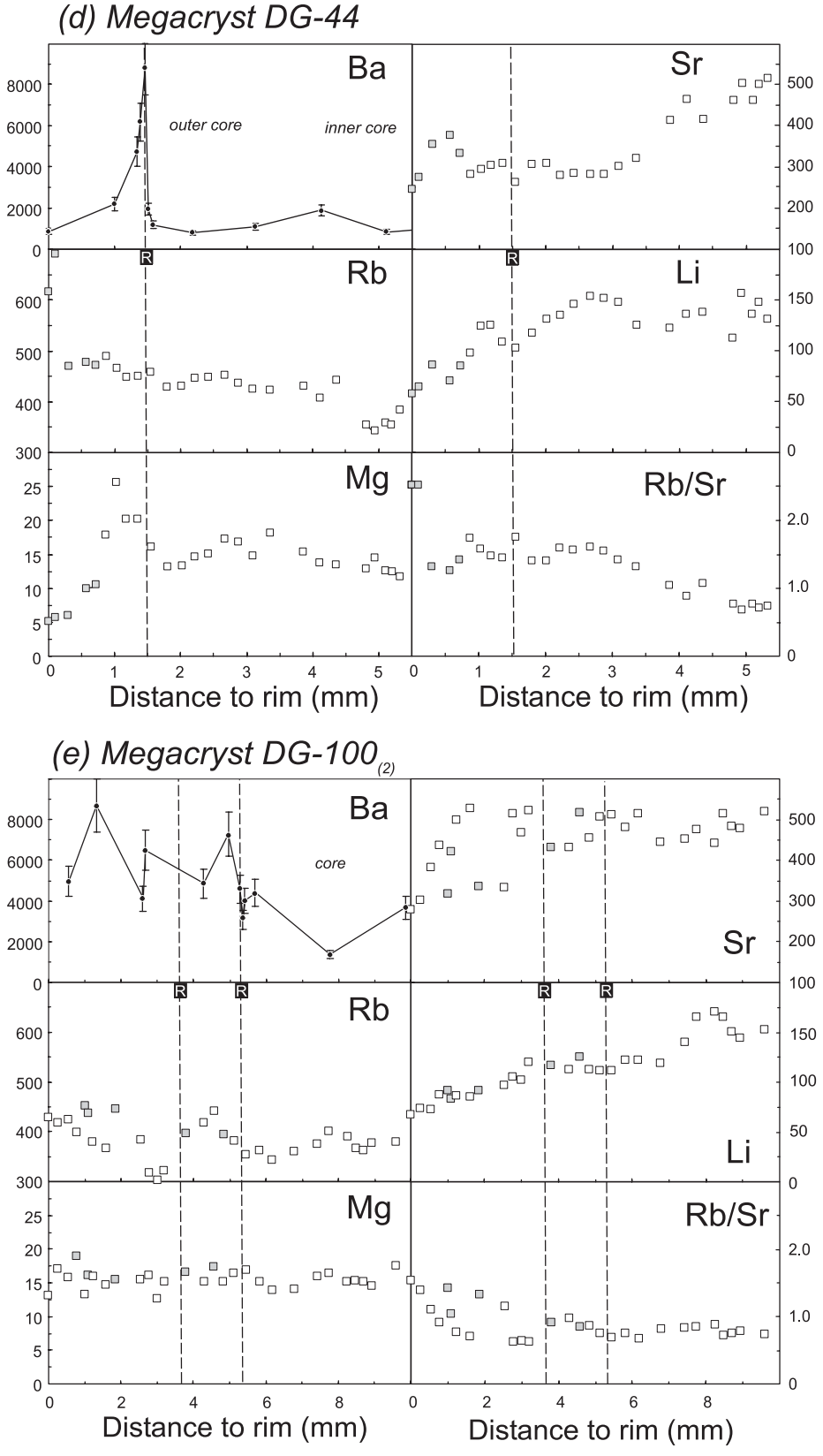

Fig. 9. Continued.

Table 2: Summary of trace element compositions (SIMS data) of K-feldspar megacrysts from the Monte Capanne pluton

Sample:	DG-44	DG-90	DG-100$_{(2)}$	DG-177$_{(2)}$	DG-56
Location:	Seccheto	Seccheto	Seccheto	Pomonte	San Piero
Rb, pristine average	429	448	373	459	405
Rb, range (pristine + turbid)	342–489	364–485	301–423	349–534	337–474
Sr, pristine average	358	321	465	359	418
Sr, range (pristine + turbid)	282–515	263–550	302–527	149–578	262–550
Ba, pristine average	n.a.	1786	n.a.	2984	2768
Ba, range (pristine + turbid)	n.a.	1148–9372	n.a.	163–9917	1070–6233
Ca, pristine average	1129	1086	1049	980	923
Ca, range (pristine + turbid)	518–1285	692–1222	712–1457	553–1759	650–1370
P, pristine average	n.a.	735	n.a.	201	448
P, range (pristine + turbid)	n.a.	51–966	n.a.	18–676	52–945
Li, pristine average	125	154	119	102	130
Li, range (pristine + turbid)	58–148	112–177	73–171	71–140	93–161
B, pristine average	2·5	1·9	1·3	3·8	2·3
B, range (pristine + turbid)	1·4–15·7	0·7–50	1–11·3	1·3–10·3	1·2–28
Cs, pristine average	10·2	7·2	4·7	6·7	6·1
Cs, range (pristine + turbid)	5·6–77	3·7–160	3·2–40	3·8–30	3·7–26
Mg, pristine average	14·8	16·8	15·6	11·5	17·2
Mg, range (pristine + turbid)	6–20·2	14·8–21·8	12·6–18·9	7–18·3	12·3–27·4

n.a., not analysed. The full dataset is available in Electronic Appendix 5 at http://www.petrology.oupjournals.org.

Ion microprobe data are not available for megacryst DG-277 (from the same locality as DG 177$_{(2)}$, Fig. 2). Ba zoning for this megacryst, determined by laser ablation ICP-MS [presented in Electronic Appendix 5; the method has been detailed by Gagnevin *et al.* (2005)] is very similar to DG-177$_{(2)}$; that is, it displays large oscillations in the inner core and an increase of Ba towards the outer core (Electronic Appendix 5).

Megacryst DG-44

Megacryst DG-44 exhibits a distinctive decrease of Sr (from 515 to 281 ppm) and increase of Rb (from 384 to 452 ppm) in the inner core region (Fig. 9), with little change in Ba (Fig. 9d). Li displays large oscillations in the core region (Fig. 9d), which contrasts with Mg (Fig. 9d). The inner rim is characterized by high Ba (Fig. 9d), but apart from Mg, other elements remains unchanged (Fig. 9d). The outer rim displays low Li and Mg, coupled with high Rb (Fig. 9d), Cs and B (Electronic Appendix 5).

Megacryst DG-100$_{(2)}$

This megacryst displays two resorption surfaces (Figs 8b and 9e). The bulk Rb/Sr ratio of megacryst DG-100$_{(2)}$ is lower than those of all the other megacrysts (Table 2; Fig. 9e). The core-to-rim decrease of Li from the inner core (171 ppm) to the outer rim (61 ppm) is noteworthy (Fig. 9e). Overall, Ba increases from core to rim (reverse zoning; Fig. 9e), although the scarcity of electron probe data precludes further comments. The core (i.e. no distinction between inner and outer core as for other megacrysts) displays wavy oscillations for most elements (Fig. 9e). Whereas the trace element composition after the first resorption surface remains unchanged, the decrease of Rb/Sr (from *c.* 0·9 to 0·6) across the second resorption surface is noteworthy (Fig. 9e), although the change is small compared with that in other megacrysts (Fig. 9e). The last 2 mm of K-feldspar growth is characterized by a continuous increase of Rb/Sr (Fig. 9e).

Sr ISOTOPIC ZONING

Sr isotopic profiles (Table 3, Fig. 11) were obtained for eight megacrysts (DG-44, -53, -56, -88, -90, -100$_{(2)}$, -177$_{(1)}$, -277), including the five megacrysts analysed for their trace element composition (see above). In the case of megacryst DG-177, slice DG-177$_{(1)}$ (parallel to {001}) was analysed rather than DG-177$_{(2)}$ (parallel to {100}) because of the better quality of the microdrilled cores. Their similar Ba zoning (Fig. 8a) suggests that they should also have similar Sr isotopic zoning. Initial $^{87}Sr/^{88}Sr$ ratios (I_{Sr}) were calculated using an age of 6·9 Ma (Table 3). The poor spatial resolution of the isotopic traverses (Fig. 11) results from the minimum spacing

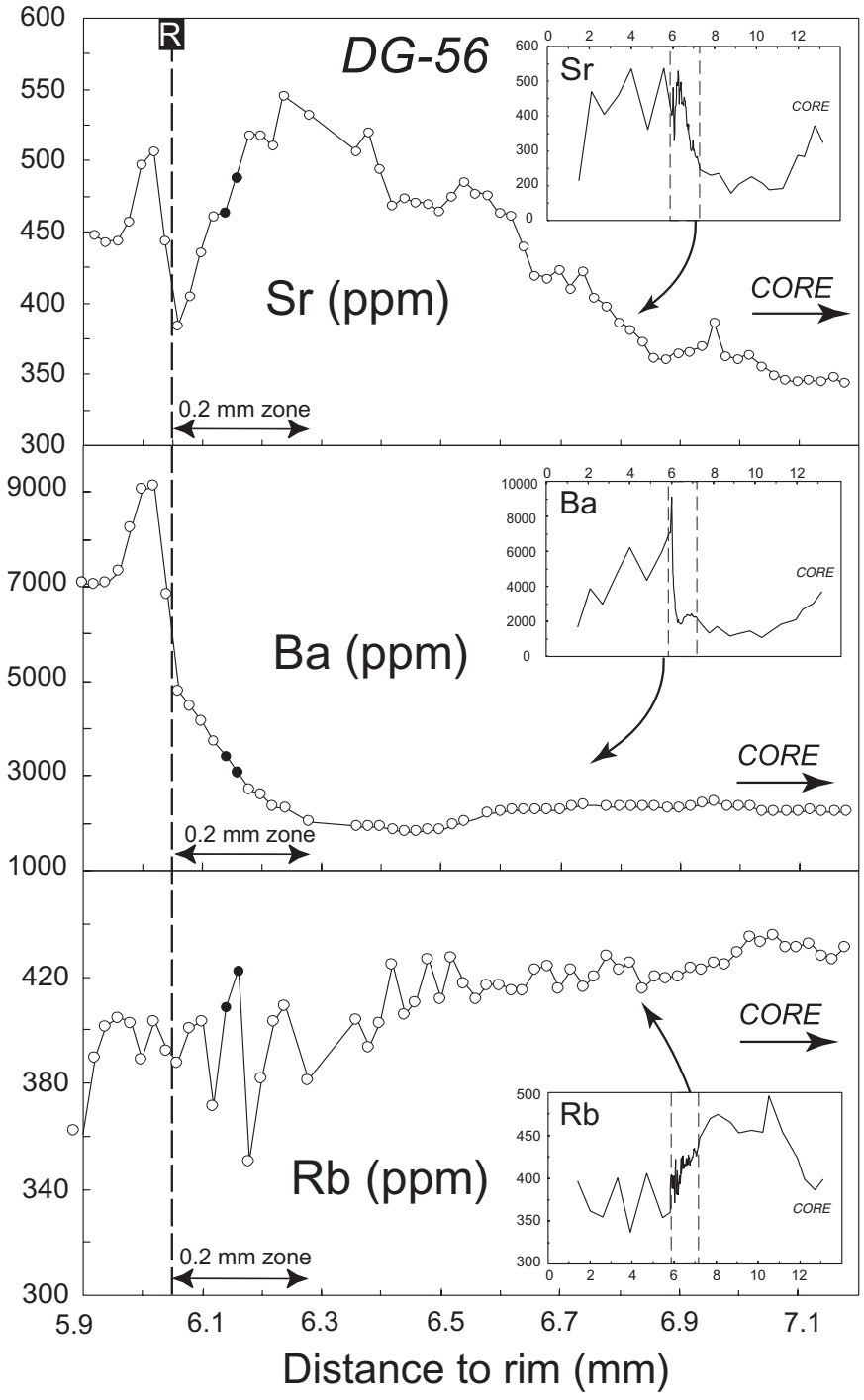

Fig. 10. Detailed SIMS profile (Sr, Ba and Rb) across the resorption surface of megacryst DG-56. Inset boxes show the main profile (Fig. 9a) with the detailed profile superimposed between dashed lines. The bold dashed line (labelled R) represents the resorption surface. The progressive rimward increase of Sr along the profile, and the increase of Ba (along with decrease of Sr) in the '0·2 mm zone' prior to resorption, is noteworthy. (See text for details.)

required between adjacent microdrill cores and the need to avoid inclusions and turbid regions.

In general, there is a decrease in Sr isotopic ratios from core to rim and, in most cases, a rise to more radiogenic compositions rimward of resorption surfaces (Fig. 11). Megacryst DG-44 displays the largest range of I_{Sr} (Table 3), from 0·7188 in the inner core to 0·7129 in the outer rim (Fig. 11a). A bulk plagioclase fraction from

Table 3: Rb–Sr isotopic composition of drilled cores in K-feldspar megacrysts from the Monte Capanne pluton

Location, sample no.	Distance* (mm)	Total Sr (ng)	Rb	Sr	$^{87}Rb/^{86}Sr$	$^{87}Sr/^{86}Sr_{(m)}$	$^{87}Sr/^{86}Sr_{(6·9)}$	$^{87}Sr/^{86}Sr_{(6·9)}$†
Seccheto, DG-44								
Core	5·5	21	249·8	140·1	5·16	0·71920 ± 5	0·71869 ± 5	0·7188 ± 2
|	3·5	23	294·9	180·6	4·73	0·71795 ± 5	0·71748 ± 5	0·7176 ± 1
|	2·4	33	307·3	219·1	4·06	0·71761 ± 5	0·71721 ± 5	0·7173 ± 1
|	2	16	321·8	214·8	4·34	0·71568 ± 6	0·71534 ± 6	0·7154 ± 2
Rim	1	16	335·6	197·1	4·93	0·71330 ± 9	0·71281 ± 10	0·7129 ± 2
Plag mantle‡	—	21427	26·9	527·7	0·15	0·71409 ± 5	0·71408 ± 5	0·71408 ± 5
Seccheto, DG-100$_{(2)}$								
Core	9	34	380·1	289·1	3·81	0·71737 ± 5	0·71699 ± 5	0·7171 ± 2
|	6	17	458·3	374·9	3·54	0·71526 ± 5	0·71503 ± 6	0·7151 ± 1
Rim	1	26	304·3	379·6	3·81	0·71519 ± 9	0·71495 ± 9	0·7150 ± 1
Plag inclusion	∼1	82	4·8	457·6	0·03	0·71475 ± 5	0·71475 ± 5	0·7148 ± 2
Seccheto, DG-53								
Core	10	31	314·3	387·5	2·35	0·71563 ± 6	0·71539 ± 6	0·7154 ± 1
|	6	36	325·0	391·2	2·41	0·71559 ± 7	0·71535 ± 8	0·7154 ± 1
|	2·5	29	248·2	334·8	2·15	0·71525 ± 8	0·71504 ± 8	0·7151 ± 1
Rim	0	33	317·2	331·5	2·77	0·71501 ± 9	0·71474 ± 10	0·7148 ± 1
Seccheto, DG-90§								
Core	9	34	461·6	279·1	4·97	0·71953 ± 7	0·71953 ± 7	0·7196 ± 2
|	4	76	412·0	210·8	5·66	0·71879 ± 5	0·71879 ± 5	0·7191 ± 1
|	2	6	383·2	266·6	4·16	0·71565 ± 15	0·71565 ± 15	0·7159 ± 4
Rim	0·5	77	399·2	492·5	2·35	0·71614 ± 6	0·71614 ± 6	0·7162 ± 1
San Piero, DG-56§								
|	4·8	25	158·1	173·0	2·65	0·71598 ± 6	0·71571 ± 6	0·7158 ± 1
|	2·7	35	314·3	511·9	1·78	0·71419 ± 21	0·71401 ± 21	0·7140 ± 2
Rim	0·7	10	243·6	278·5	2·53	0·71493 ± 5	0·71468 ± 5	0·7148 ± 2
Pomonte, DG-88								
|	11·5	28	356·1	348·2	2·96	0·71559 ± 6	0·71530 ± 6	0·7154 ± 1
Rim	0·5	20	321·5	260·7	3·57	0·71532 ± 6	0·71497 ± 6	0·7150 ± 1
Pomonte, DG-177$_{(1)}$								
|	6·5	43	286·7	241·0	2·43	0·71650 ± 5	0·71626 ± 5	0·7163 ± 1
|	4·5	22	357·8	277·9	3·73	0·71535 ± 5	0·71491 ± 6	0·7150 ± 1
|	3·7	8	333·8	304·9	2·64	0·71505 ± 6	0·71489 ± 7	0·7151 ± 1
|	1·6	17	296·2	296·8	2·90	0·71515 ± 6	0·71476 ± 6	0·7148 ± 1
Rim	1	10	255·9	228·0	3·25	0·71528 ± 5	0·71496 ± 5	0·7151 ± 2
Pomonte, DG-277								
Core	9·5	13	319·6	216·7	4·27	0·71774 ± 6	0·71732 ± 6	0·7175 ± 2
|	6·8	24	469·9	495·8	2·74	0·71586 ± 6	0·71558 ± 6	0·7157 ± 1
|	5	5	69·3	65·5	3·06	0·71518 ± 9	0·71488 ± 6	0·7152 ± 4
|	2·5	16	118·7	173·5	1·98	0·71503 ± 6	0·71484 ± 6	0·7149 ± 2
Rim	0·5	3	287·2	80·4	10·34	0·71599 ± 6	0·71498 ± 6	0·7155 ± 6

Rb and Sr concentrations were determined by isotope dilution. Total amount of Sr is equal to the sample weight multiplied by the measured Sr concentration. Denoted uncertainty is 2σ error. Subscripts: (m), measured $^{87}Sr/^{86}Sr$; (6·9), initial $^{87}Sr/^{86}Sr$ calculated at 6·9 Ma.

*Distance relative to the rim of the megacrysts.

†Calculated after blank correction.

‡Analysis performed on a bulk mineral separate.

§Analysis of the megacryst core was not possible because of its high degree of turbidity.

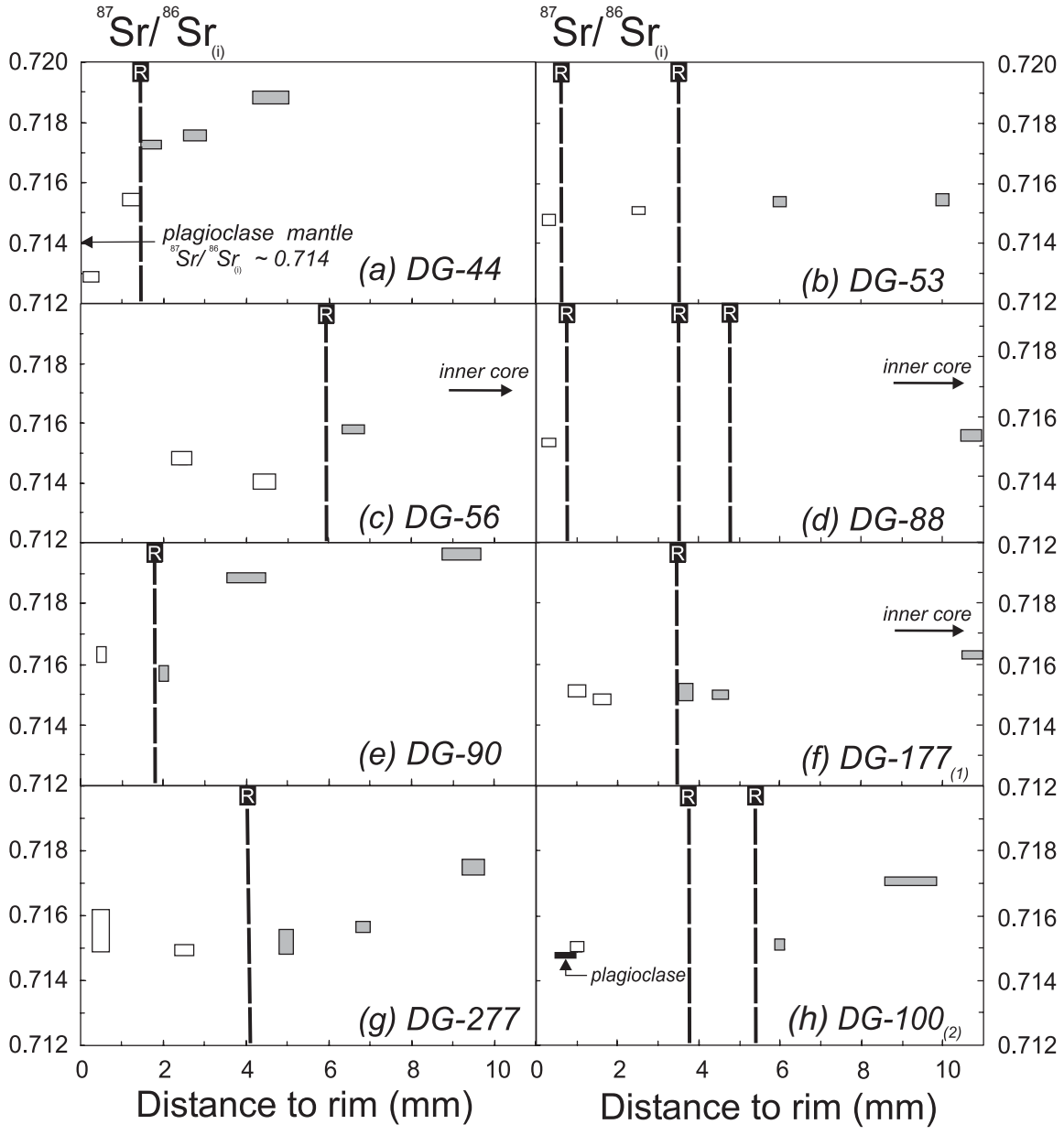

Fig. 11. Initial Sr isotopic profiles (calculated for 6·9 Ma) from analyses of microdrilled cores in eight Kfm. Microdrill locations for DG-56 are shown in Fig. 4, and the others are shown in Electronic Appendices 1–3 at http://www.petrology.oupjournals.org. (See Figs 8 and 9 for EMPA and SIMS traverses on the same samples.) The diameter of microdrilled cores is indicated by the bar length, and the bar heights are proportional to the 2σ error. The bold dashed lines (labelled R) represent the resorption surfaces.

the rapakivi mantle also displays relatively low I_{Sr} (0·7141) (Table 3). Megacrysts DG-90, -100$_{(2)}$, -277 and -177$_{(1)}$ have similar I_{Sr} profiles (Fig. 11); that is, high I_{Sr} in the inner cores (up to I_{Sr} = 0·7196; Fig. 11e) decreases rimwards towards the outer cores. A plagioclase inclusion near the rim of megacryst DG-100$_{(2)}$ displays similar, although slightly lower I_{Sr} (0·7148) than the K-feldspar rim (0·7150) (Fig. 11f), indicating that K-feldspar and plagioclase crystallized close to isotopic equilibrium. Megacrysts DG-53 and DG-88 display little core-to-rim variations (Fig. 11b), although I_{Sr} slightly decreases in both cases (i.e. from 0·7158 to 0·7148 in DG-53 and from 0·7154 to 0·7150 in DG-88; Table 3).

DISCUSSION

In spite of careful sampling, an unavoidable uncertainty arises from the possibility that the 'true' centre plane of the K-feldspar megacrysts has not been sectioned (see also Gagnevin *et al.*, 2005). In consequence, it is possible

that the earliest phase of K-feldspar growth is underrepresented, although there is no evidence that this is the case. Bearing this uncertainty in mind, the chemical and isotopic zoning features described above are discussed and interpreted in the following sections. First, the role of solid-state diffusion is addressed and found to be relatively unimportant. Thus the observed chemical and isotopic zoning is discussed in terms of its petrogenetic significance, treating the megacryst inner cores, outer cores and rims in sequence and evaluating the importance of disequilibrium growth. The detailed profile across the resorption surface in one megacryst is then discussed.

Extent of diffusive equilibration and constraints on timescales

Sr isotopic zoning

It is essential to evaluate the possible role of gradient-driven diffusive equilibration between crystals and (high-temperature) melts to produce the isotopic profiles (e.g. Feldstein *et al.*, 1994; Davidson & Tepley, 1997). For example, the continuous core to rim decrease of I_{Sr} (e.g. Fig. 11) can be explained by diffusive equilibration of a megacryst of uniform isotopic composition (equivalent to the core) immersed in a melt of less radiogenic composition. To evaluate the extent of diffusive equilibration, we used a model of diffusion in a sphere using equation (6.18) of Crank (1975) at a temperature of 800°C, which is the upper limit of zircon and monazite saturation temperatures calculated for the monzogranite facies (Gagnevin *et al.*, 2004). For K-feldspar, the calculated Sr chemical diffusivity at 800°C is $7{\cdot}50 \times 10^{-16}$ cm^2/s (Cherniak, 1996). Calculated diffusion profiles for megacryst DG-44 (which displays the largest range of isotopic variation; Fig. 9) indicate that a timescale of *c.* 20 Myr at 800°C would be required to account for the observed isotopic profiles (Fig. 12). Even longer timescales were modelled in other megacrysts (up to 100 Myr for megacryst DG-53; not shown). We consider these timescales unrealistic in the light of other studies on the crystallization history of granitic plutons (e.g. Neves & Vauchez, 1995; Harris *et al.*, 2000) and in view of the young age of the intrusion (6·9 Ma). Further constraints on timescales can be obtained using feldspar growth rates. K-feldspar megacrysts exhibit variable crystal size (between 3 cm and 7 cm wide parallel to {100}). Using a rather slow (and constant) growth rate of 7×10^{-13} cm/s (Davies *et al.*, 1994), the calculated growth intervals for Kfm vary between 0·1 and 0·3 Myr, which contrast with the timescales for diffusion calculated above (>10 Myr). It is possible that the megacrysts may have grown at an even faster rate (e.g. 10^{10}–10^{11} cm/s; e.g. Tepley *et al.*, 1999; Davidson *et al.*, 2001) relative to other phases; therefore their growth interval may have been even shorter (i.e. <1–10 kyr).

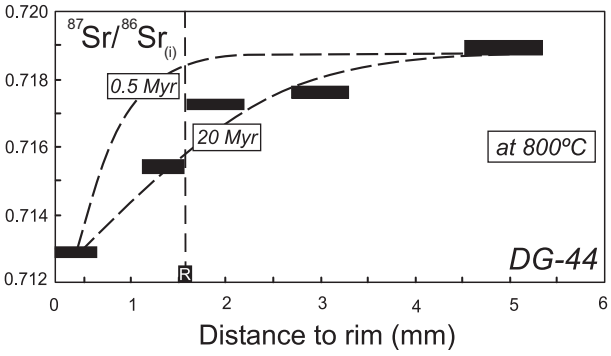

Fig. 12. Diffusion profiles (dashed curves) calculated using equation (6.18) of Crank (1975), which evaluates the extent of equilibration of a sphere immersed in a liquid of different isotopic composition. Sr chemical diffusivity is from Cherniak (1996). The Sr isotope profile for megacryst DG-44 (data boxes as in Fig. 11) is matched by the diffusion profile at *c.* 20 Myr at 800°C. This is an unrealistic timescale for a plutonic system (<0·5–1·0 Myr, e.g. Neves & Vauchez, 1995), therefore ruling out post-crystallization diffusive equilibration as an explanation for the observed isotopic zoning. The dashed line (labelled R) represents the resorption surface.

Given the likely growth intervals, the observed Sr isotopic profiles are interpreted to reflect changes in magma composition over time (i.e. growth zoning), rather than variable re-equilibration as a result of diffusion.

Trace element zoning

Evaluating the effect of diffusion on the trace element profiles is also critical to assess their primary character. Diffusive equilibration will tend to obliterate primary chemical discontinuities over time and therefore has the potential to provide maximum estimates of crystal residence time in the magma at a given temperature if the initial state of the crystal is known, or can be supposed (e.g. Zellmer *et al.*, 1999). K-feldspar rimward of the resorption surfaces is characterized by high Ba and Sr contents compared with the outer cores (Fig. 9a–c). This could, potentially, reveal information on the extent of diffusive re-equilibration between zones of contrasting composition within the megacrysts.

Several diffusion scenarios may account for the 0·2 mm zone (see above) along the detailed profile obtained across the resorption surface of megacryst DG-56 (Fig. 10), as follows.

(1) Intra-crystalline diffusive equilibration across the resorption surface between zones of contrasting composition could explain the Ba profile (Fig. 10b). However, the Sr profile is sharply 'broken' across the resorption surface. The first spot rimward of the resorption surface has a higher Sr concentration than the last spot coreward of the resorption surface (Fig. 10a). This is not to be expected in the case of intra-crystalline diffusion, because diffusion should smooth elemental variations, which is not observed here (Fig. 10). Excessively

long timescales would also be required: using the K-feldspar diffusivity model of Cherniak (2002), the characteristic diffusion time to account for the Ba profile in the 0·2 mm zone at a temperature of 900°C is *c.* 0·8 Myr. Finally, the observed oscillations in Rb (even at low Cs) in the 0·2 mm zone (Fig. 10c) argue against diffusion, as Rb should have become totally re-equilibrated across the resorption surface considering its considerably faster diffusivity in alkali feldspar (Giletti, 1991).

(2) The 0·2 mm zone could represent the time elapsed between dissolution and renewed crystallization with the zoning controlled by crystal–melt diffusional exchange at high temperature. Decoupling Ba from Sr in the 0·2 mm zone (Ba increases, Sr decreases; Fig. 10) could be explained if Sr was strongly fractionated by plagioclase crystallization (for which Ba is not compatible) after resorption. Although attractive, we rule out this hypothesis simply because Ba and Sr are coupled after resorption (both increase; Fig. 10), despite abundant plagioclase and apatite, which would strongly fractionate Sr (Fig. 10).

(3) Another possibility is that dissolution was driven by diffusion (diffusive crystal dissolution; Zhang *et al.*, 1989); the 0·2 mm zone would thus represent a 'fossilized' feldspathic melt (as a result of K-feldspar dissolution) that was exchanging elements with the granitic melt via diffusion (Watson, 1982; Bussy, 1990*b*). However, Sr and Ba should both diffuse uphill towards less polymerized melts (Watson, 1982; Zhang *et al.*, 1989; Lesher, 1994), but the exact opposite is observed here, as Ba and Sr behave antithetically (Fig. 10). Furthermore, such Ba-rich and Sr-poor melts are not recorded in the MC pluton, where Ba and Sr are correlated (Dini *et al.*, 2002; Gagnevin *et al.*, 2004), therefore ruling out this possibility.

Having ruled out these three diffusion scenarios, we conclude that diffusion was limited, during both dissolution and subsequent megacryst growth. A more complex scenario is developed below.

Element partitioning

Modelling based on crystal–melt equilibrium has been extensively used for feldspar phenocrysts, and has proved to be particularly efficient in modelling mixing (Singer *et al.*, 1995; Ginibre *et al.*, 2002) and fractionation paths (Mason *et al.*, 1985; Blundy & Shimizu, 1991; Brophy *et al.*, 1996). However, trace element modelling requires the precise knowledge of the mineral–melt partition coefficients. The large range of reported partition coefficients for Ba, Sr and Rb in feldspars arises from the fact that the partitioning is strongly dependent on the crystal structure and the temperature (Long, 1978; Blundy & Wood, 1991) and/or the melt structure (Carron & Lagache, 1980), which varies from case to case (e.g. Leeman & Phelps, 1981; Nash & Crecraft, 1985). Icenhower & London (1996) carried out experiments (at $P < 2$ kbar and $T =$ 650–750°C), based on *in situ* growth of K-feldspar in peraluminous melts, and under similar P–T conditions to those inferred for the MC pluton emplacement (1–2 kbar and >650°C; Bussy, 1991; Dini *et al.*, 2002). The Icenhower & London experiments produced K-feldspar compositions (90 mol % Or) similar to Kfm investigated in this study (62–94 mol % Or; Table 1; Electronic Appendix 4).

$D(\mathrm{Ba})^{\mathrm{Fsp/gl}}$ and $D(\mathrm{Rb})^{\mathrm{Fsp/gl}}$ strongly depend on the major element composition (mol % Or) of the K-feldspar [see the equations of Icenhower & London (1996) for formulae], which varies from 62 to 94 mol % Or for zoned Kfm from the MC monzogranite. Excluding the megacryst outer rim (Fig. 8a and b) and local abundance of patch perthites (Fig. 6), the range of variation in individual megacrysts is small (Fig. 8a and b). For example, the average Or content in the core region is 78·7 ± 1·3 mol % and 76·1 ± 2·0 mol % for DG-56 and DG-90, respectively. The Rb and Ba variations in K-feldspar are thus inferred to reflect the variations in the melt.

$D(\mathrm{Sr})^{\mathrm{Fsp/gl}}$ is independent of K-feldspar composition (Icenhower & London, 1996), but the reason for the range of reported partition coefficient [$D(\mathrm{Sr})^{\mathrm{Fsp/gl}} =$ 10–14] is unclear. Long (1978) noted a dependence on temperature and Or content in synthetic granitic melts. Pressure may be an issue to consider, as pressure dependence for Ba partitioning has been reported (Guo & Green, 1989). However, the Guo & Green experiments were run at pressures from 10 to 25 kbar and with different starting materials (i.e. alkaline melts), whereas the MC pluton has calc-alkaline affinities and a crustal source inferred to be at a maximum pressure of 5–6 kbar (Bussy, 1990*a*), although this is largely speculative (Gagnevin *et al.*, 2004). Parallel variations of Ba, and especially Rb, lead us to conclude that Sr zoning reflects variations in the melt (and associated temperature and/or H_2O activity) during growth.

The megacryst inner cores

Evidence of crystal fractionation and mixing prior to K-feldspar crystallization

Several petrographic observations suggest that the Kfm crystallized from melts that had already undergone earlier episodes of crystal fractionation. The best illustration of this is the extensive occurrence of euhedral to subhedral inclusions of plagioclase with subordinate biotite, apatite and quartz in the megacryst cores, showing that these phases were crystallizing simultaneously with K-feldspar (Hibbard, 1965; Franzini *et al.*, 1974). On textural grounds, Bussy (1990*a*) suggested that K-feldspar started to crystallize after *c.* 40–50% crystallization

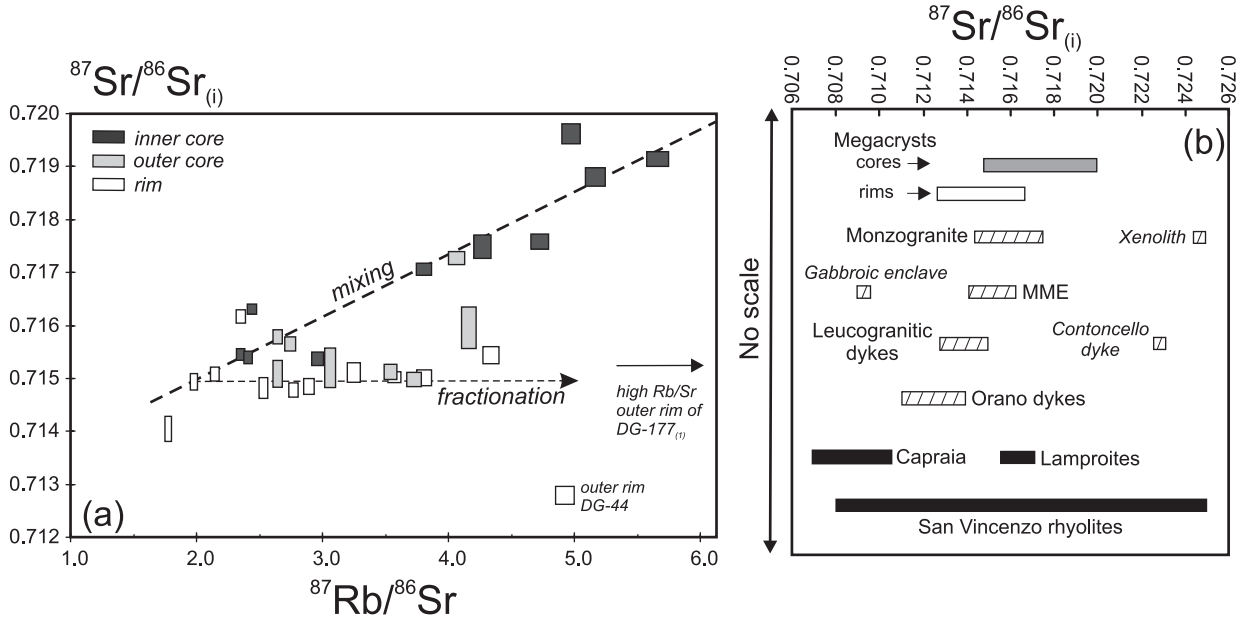

Fig. 13. (a) Initial $^{87}Sr/^{86}Sr$ vs $^{87}Rb/^{86}Sr$ diagram for the Monte Capanne Kfm. The 2σ error is represented by the box dimensions. Larger errors arise from smaller samples and hence larger blank contributions. It should be noted that the distinctive positive $^{87}Rb/^{86}Sr$–$^{87}Sr/^{86}Sr$ correlation exhibited by the megacryst inner cores (dark boxes) has no age significance, but rather reflects mixing (bold dashed best-fit line) between radiogenic crustal and mantle-derived magmas. The rims (white boxes) display a wide range in Rb/Sr ratio but a much more restricted spread in I_{Sr}, following a fractionation trend (fine dashed line). (See text for further discussion.) (b) Range of initial Sr isotopic values in the Kfm compared with whole-rock data for the MC pluton and related magmatic products, Capraia volcanics, lamproites (orendites) and San Vincenzo rhyolites. The megacryst rims extend towards less radiogenic compositions (mantle-derived, similar to Capraia) whereas the cores have more radiogenic isotopic values (crustal; extending towards the crustal xenolith and the Cotoncello dyke). Sources of data: Peccerillo *et al.* (1988); Ferrara *et al.* (1989); Dini *et al.* (2002); Gagnevin *et al.* (2004); G. Poli, unpublished data (2002).

of plagioclase, biotite, quartz, zircon and apatite. Calculated melt compositions [using $D(Sr)^{Kfsp/gl} = 10$ and $D(Rb)^{Kfsp/gl} = 0{\cdot}8$; Icenhower & London, 1996] in equilibrium with the inner cores of megacrysts DG-44, DG-56 and DG-$100_{(2)}$ have higher Rb/Sr (9·1–11·5) than (1) the MC monzogranite (Rb/Sr = 1·0–1·6) and (2) typical anatectic melts from the Tuscan Magmatic Province (Rb/Sr = 0·9–8·8); that is, the Roccastrada rhyolites (Pinarelli *et al.*, 1989), the Cotoncello dyke (Dini *et al.*, 2002) and the Giglio leucocratic facies (Poli *et al.*, 1989; Poli, 1992). This suggests that the K-feldspar megacrysts crystallized from melts already depleted in feldspar-compatible elements (e.g. Sr) and enriched in feldspar-incompatible elements (e.g. Rb), which can be explained by abundant plagioclase fractionation (Halliday *et al.*, 1991).

Low P in the inner core of megacryst DG-56 is noteworthy (Fig. 9a), and coincides with the occurrence of coarse apatite crystals. As apatite is stable in Ca-rich metaluminous melts (Dini *et al.*, 2004), the core of DG-56 strongly suggests that mixing between mantle-derived, metaluminous melts and anatectic, peraluminous melts had already occurred before the K-feldspar megacrysts began to crystallize. The significance of P zoning is discussed in detail below.

Evidence for crustal contamination

The megacryst inner cores ($I_{Sr} = 0{\cdot}7154$–$0{\cdot}7196$, Table 3) define a mixing trend in an isochron diagram (Fig. 13a), which has no age significance (the slope of the mixing curve corresponds to an age of *c.* 80 Ma). The decrease of I_{Sr} in the most radiogenic megacrysts, that is, DG-44 (from 5 to 2 mm; Fig. 11a) and DG-90 (from 9 to 4 mm; Fig. 11f), indicates that the high I_{Sr}–$^{87}Rb/^{86}Sr$ melt component was diluted as crystallization proceeded. It is proposed that the radiogenic component results from partial assimilation of Sr-radiogenic wall-rocks ($I_{Sr} > 0{\cdot}720$) prior to K-feldspar crystallization, as suggested by abundant partially digested metapelitic xenoliths dispersed throughout the pluton. These 'surmicaceous enclaves' are consistent with partial melting of an Al-rich metasedimentary protolith through muscovite and biotite dehydration-melting reactions (e.g. Van Bergen & Barton, 1984; Montel *et al.*, 1991).

Partially digested xenoliths may also represent restitic material transported from the magma source region to the level of emplacement (Chappell *et al.*, 1987). Although intensely debated in the literature (e.g. Maas *et al.*, 1997; White *et al.*, 1999, and references therein), we favour the hypothesis of partial assimilation of metasedimentary wall-rocks (e.g. Van Bergen & Barton, 1984; Maury &

Didier, 1991; Feldstein *et al.*, 1994; Maas *et al.*, 1997, 2001; Nitoi *et al.*, 2002), as crustal contamination can also explain the distinctive low Nd and high Sr isotopic compositions observed in some MME (whose origins have been clearly attributed to magma mixing; see above). MME form a trend towards a garnet-bearing mica schist xenolith (sampled in the granite porphyry in Marciana Marina; Fig. 2) (Gagnevin *et al.*, 2004). From its petrography, this xenolith is similar to lower Palaeozoic mica schists in eastern Elba (Monte Calamita; Keller & Pialli, 1990), as well as the Lardarello geothermal field and deep boreholes in Tuscany (Bagnoli *et al.*, 1979).

Evidence for magma recharge with silicic melts

Magma recharge with more mafic material has often been invoked to explain multiple resorption events (Singer *et al.*, 1995; Ginibre *et al.*, 2002) and rimward decrease of I_{Sr} in plagioclase phenocrysts (e.g. Davidson & Tepley, 1997; Tepley *et al.*, 1999). Recharge with silicic magmas, although less often reported, can also occur (e.g. Hervig & Dunbar, 1992; Knesel *et al.* 1999; Anderson *et al.*, 2000; Ginibre *et al.*, 2002). The marked increase of Rb/Sr ratio and decrease of Ba in the inner cores of megacrysts DG-44 (Fig. 9d) and DG-56 (Fig. 9a), as well as the decrease of I_{Sr} in the inner core region of megacrysts DG-44 (Fig. 11a) and DG-90 (Fig. 11a), suggest that recharge with high Rb/Sr and high I_{Sr} (*c.* 0·717) silicic melts occurred and became the dominant process governing the trace element and isotopic zoning. The depleted signature of the inferred melt may have been acquired by extensive crystal fractionation, either in the same magma chamber or in a separate level of magma storage.

The lack of zoning in Sr and Ba in the inner core of DG-90 (Fig. 9b) may point to the possibility that the 'true' megacryst core has not been sampled (see above). Alternatively, this may reflect the continuous input of depleted silicic magmas during the growth of the magma chamber (R. S. J. Sparks, personal communication, 2002). Wavy oscillations in Rb and Li in the inner core of megacryst DG-90 (from 8 to 4 mm; Fig. 9b) may be related to convective transport into thermal and compositional gradients in the magma chamber (e.g. Halama *et al.*, 2002). Sharper oscillations for all elements in the inner core of megacryst DG-177$_{(2)}$ (i.e. from 10 to 12 mm; Fig. 9c) are possibly due to alteration, as is also suggested by slightly higher B contents (>9 ppm; Electronic Appendix 5).

The megacryst outer cores

The outer cores of DG-56 (Fig. 9a), DG-90 (Fig. 9b) and DG-177$_{(2)}$ (Fig. 9c) display a clear decrease of Rb/Sr, Li and P and increase of Ba. This is coupled with a decrease of I_{Sr} in megacryst DG-90 (Fig. 11e) and less clearly in megacrysts DG-177$_{(1)}$ (Fig. 11d) and DG-277 (Fig. 11 g). We propose that these features reflect the influx of more primitive melts (with high Ba, low Rb/Sr and I_{Sr}) into the magma chamber. The lack of this low Rb/Sr zone in megacryst DG-44 suggests that it may have been removed by dissolution during resorption.

Noticeably, the increase of Ba in the outer core of DG-90 and DG-177$_{(2)}$ is followed by a decrease back to concentrations similar to those of the inner cores (Fig. 9b and c). This suggests that intermittent recharge with silicic melts may have occurred during growth of the outer core (Gagnevin *et al.*, 2005), unless the decrease in Ba reflects a change in partitioning caused by the influx of mafic magma (e.g. Shimizu & Le Roex, 1986). Ba zoning in the outer core is further discussed below in the light of the detailed ion microprobe traverse in DG-56.

The megacryst rims

Significance of resorption surfaces

The irregular and indented shapes of the resorption surfaces (Fig. 5b) provide evidence for dissolution and regrowth in higher temperature melts during magma mixing (Stimac & Wark, 1992; Cox *et al.*, 1996). The patchy texture in the megacryst rims suggests a complex three-dimensional framework typical of dissolution textures (e.g. Andersson & Eklund, 1994). Plagioclase mantling around K-feldspar also suggests magma mixing (Hibbard, 1981; Vernon, 1990). This texture is common in the MC monzogranite (Fig. 5a) and its MME (Bussy, 1990*a*). Wark & Stimac (1992) demonstrated experimentally that diffusion between melts of different bulk composition is an important process in producing this texture.

We emphasize that the formation of resorption surfaces follows similar, diffusion-limited, dissolution of K-feldspar. The formation of a plagioclase mantle (instead of renewed K-feldspar growth) would be controlled by the degree of chemical and thermal disequilibrium between the feldspar melt and the magma (Glazner *et al.*, 1988; Stimac & Wark, 1992; Wark & Stimac, 1992); that is, dissolution at high temperature would produce a resorption surface instead of a plagioclase mantle. Bussy (1990*b*) described a 'poikilitic K-feldspar mantle' with numerous inclusions within some MME in the MC pluton, closely resembling the rim of zoned megacrysts in the monzogranite.

Apart from Ba, there are no clear changes in trace element abundances across the resorption surfaces (Fig. 9). In most cases, however, a resorption surface corresponds to a change in zoning trend (Fig. 9). This is particularly well illustrated in megacryst DG-177$_{(2)}$ (Fig. 9d). Thus rather than corresponding to a sudden change in magma composition (Cox *et al.*, 1996), resorption of K-feldspar is related to variations in P–T conditions during crystallization.

Evidence for magma mixing with mafic magmas

The occurrence of resorption surfaces (Fig. 5b) and associated sharp Ba zoning (Fig. 8), cannot be explained by fractionation of Ba-poor crystal phases (Mehnert & Büsch, 1981; Long & Luth, 1986; Vernon, 1986), but rather, reflects magma mixing with mafic magma (e.g. Cox *et al.*, 1996), as attested by (1) low Rb/Sr and high Ba contents (Fig. 9a–c) and (2) low I_{Sr} in the rims compared with the cores (Figs 11a–c and 13b). Despite having the least radiogenic Sr isotopic composition (Fig. 11a) and a marked Ba spike (Fig. 8a), there is no marked change in Sr across the resorption surface of megacryst DG-44 (Fig. 9d). This can be explained by the simultaneous growth of plagioclase (incompatible for Ba), consistent with the occurrence of a plagioclase mantle in this megacryst (Gagnevin *et al.*, 2001).

If magma mixing was the cause of resorption, the diversity of the zoning profiles at the rims needs to be better explained. Two contexts are envisaged through which crystal resorption can occur, as detailed below.

Evidence for resorption in an MME

Several lines of evidence suggest that megacrysts DG-90 and DG-44 may have been captured and dissolved in a mafic enclave: they have (1) a plagioclase mantle (common in MME) (Figs 8a and b, 9b–d), (2) abundant acicular apatite rimward of the resorption surface (suggesting rapid growth), (3) only one resorption surface (i.e. only one dissolution event) and (4) a low rim/core volume ratio, suggesting depletion of K-feldspar components in the more basic environment of an MME. Megacrysts DG-44 and DG-90 were collected in the monzogranite, therefore transfer out of an enclave must have occurred at some stage. Thick plagioclase mantling, such as in megacryst DG-44 (Fig. 5a), would simply armour the K-feldspar against further growth.

Transfer of phenocrysts from an MME back into the host has been documented in other cases (e.g. Barbarin, 1990; Waight *et al.*, 2001) resulting from partial desegregation and dispersal of enclave material in the granitic host. Megacryst DG-56 does not exhibit a plagioclase mantle and its high rim/core ratio is noteworthy (Fig. 9a). Based on Ba zoning, an inner rim and an outer rim can be clearly distinguished, using both EMPA and SIMS data (Fig. 9a, see fine dashed line). This discontinuity may reflect transfer out of an MME occurred during rim crystallization, reconciling the occurrence of acicular apatite along the resorption surface.

Evidence for prolonged residence time in more mafic melts

Whereas some zoned Kfm suggest capture by an enclave (see above), Kfm displaying two or more resorption surfaces require a more complex scenario. In particular, they have (1) higher rim/core volume ratios, (2) abundant plagioclase inclusions after the first resorption surface, (3) pronounced patchy zoning (i.e. advanced dissolution) and (4) thick rims of Ba-rich K-feldspar (e.g. DG-53, DG-88 and DG-95; Fig. 8a and b). These megacrysts do not generally display acicular apatite along the resorption surfaces, apart from the last resorption event, where they may occur (e.g. in DG-100). Interestingly, they also have relatively low I_{Sr} (0·7155–0·7175) in the core inner regions (Fig. 11b–f), as well as a marked Ba reverse zoning (except for DG-95; Fig. 8a and b). These features are not restricted to megacrysts that exhibit several resorption surfaces. For example, the rim of megacryst DG-$177_{(2)}$ lacks acicular apatite and displays pronounced reverse zoning (Fig. 8a).

The above-cited features are compatible with prolonged residence in hybrid melts contaminated with a low I_{Sr}, mantle-derived, component. The occurrence of several resorption surfaces, coupled with abundant plagioclase inclusions, points to fluctuating crystallization conditions (Vaniman, 1978; Vernon, 1986) that could be related to (1) movement of crystals through inner (or deeper), more liquid, parts of the magma chamber, (2) the thermal imprint of successive pulses of mafic magma at the base of the magma chamber (Wiebe, 1993; Wiebe *et al.*, 1997) and/or (3) complex crystal pathways as a result of the chaotic dynamics of the interaction process (Perugini & Poli, 2001).

Evidence for crystal fractionation

The continuous decrease of Ba and Sr at the rim of megacrysts DG-56, DG-90 and DG-$177_{(2)}$ is noteworthy (Fig. 9a–c). The outer rims typically record the lowest Ba and Sr concentrations (211–798 ppm Ba; 148–290 ppm Sr), which are similar to those of poikilitic K-feldspars in the monzogranite (674–1268 ppm Ba; 172–309 Sr ppm; Franzini *et al.*, 1974). Low Ba and Sr is generally mirrored by an increase of mol % Or (84–94) (Fig. 8) towards the outer rims, which suggests that the megacryst outer rims crystallized simultaneously with the groundmass K-feldspar at late stages of crystallization (e.g. Mehnert & Büsch, 1981). The role of crystal fractionation is also supported by the rather limited range of Sr isotopic composition (0·7148–0·7152) in most megacryst rims, compared with the wider range of trace element compositions (Figs 9 and 13a).

Possible intervention of a hydrothermal fluid

Closed-system crystal fractionation cannot account for the slight increase of I_{Sr} in the outer rim of DG-56 (Fig. 11c), DG-$177_{(1)}$ (Fig. 11d) and DG–277 (Fig. 11 g). We suggest that a hydrothermal fluid with a more radiogenic Sr isotopic signature may have contributed to the

bulk magma at late stages of crystallization, which is also supported by bulk-rock oxygen isotopic data (Taylor & Turi, 1976) and Pb isotopic data from the megacrysts (Gagnevin *et al.*, 2005).

Sr isotopic constraints on the nature of the mantle-derived magma

The rim and the plagioclase mantle of megacryst DG-44 have unradiogenic Sr compositions (I_{Sr} is 0·7128 and 0·7141, respectively) relative to the core (Fig. 11a). This can be compared with the wide range of Sr isotopic ratios displayed by mantle-derived magmas within the TMP (e.g. Peccerillo *et al.*, 2001; Poli *et al.*, 2002), ranging from moderately depleted (I_{Sr} = 0·7074–0·7102; Fig. 13b) high-K calc-alkaline volcanics (in Capraia) to enriched (I_{Sr} = 0·7158–0·7164; Fig. 13b) lamproitic magmas (in Orciatico and Montecatini). The San Vincenzo rhyolites encompass almost the same range of I_{Sr} (0·7081–0·7247; Fig. 13b) (Ferrara *et al.*, 1989) and display similar Sr isotopic variations within individual minerals (I_{Sr} = 0·7087–0·7247) (Feldstein *et al.*, 1994).

I_{Sr} values from the rim of DG44 are thus compatible with a high-K calc-alkaline affinity for the mantle-derived end-member involved in magma mixing, which was expected in the light of earlier whole-rock investigations of Tuscan granitoids (e.g. Poli, 1992; Innocenti *et al.*, 1997; Dini *et al.*, 2002; Gagnevin *et al.*, 2004). The low I_{Sr} at the rim of megacryst DG-44 is similar to the hybrid Orano dykes (Fig. 13b; Gagnevin *et al.*, 2004). Intermediate Sr isotopic values (0·7140–0·7161) in the rim (Fig. 13b) are similar to MME whole-rock values (I_{Sr} = 0·7137–0·7159, excluding the gabbroic enclave; Fig. 13b) (Gagnevin *et al.*, 2004), and overlap with the monzogranite (0·7148–0·7172). Isotopic and trace element heterogeneities are common in MME (Didier & Barbarin, 1991), and reveal a combination of processes, such as magma mixing, *in situ* crystallization and diffusive exchange with the host (e.g. Poli & Tommasini, 1991; Elburg, 1996; Wiebe *et al.*, 1997; Waight *et al.*, 2001) that may be difficult to distinguish from one other (Gagnevin *et al.*, 2004).

Insights from P zoning

The three megacrysts for which P analyses are available (DG-56, DG-90 and DG-177$_{(2)}$) have comparable zoning patterns. In each case the rims exhibit low P values, but, in detail, some important differences are evident. A rapid decrease of P occurs at the resorption surface in megacryst DG-56 (Fig. 9a), but occurs in the outer core in DG-90 (Fig. 9b) and DG-177$_{(2)}$ (Fig. 9c). Furthermore, the decrease of P in megacryst DG-177$_{(2)}$ is observed over *c.* 2 mm of crystal growth (Fig. 9c), whereas it is a much sharper feature in both DG-56 and DG-90 (Fig. 9a and b).

Apatite is the main control of the P budget during crystallization, and occurs as inclusions in almost all Kfm. In zoned Kfm, the occurrence of resorption surfaces is sometimes associated with minute acicular apatite crystals, which is the case for megacrysts DG-56 and DG-90, but not for DG-177$_{(2)}$. Acicular apatites are common in MME (e.g. Vernon, 1990) and result from rapid growth at high degrees of undercooling (Wyllie *et al.*, 1962). Their presence at resorption surfaces reflects steep P gradients at the crystal–liquid interface (Bacon, 1989), hence providing a first-order explanation for the sharp decrease of P in DG-56. However, this cannot account for the fact that the decrease in P is not necessarily associated with the occurrence of apatite inclusions (in DG-177$_{(2)}$ and DG-90; Fig. 9b and c).

In peraluminous granites (such as the MC pluton), $D(P)^{Kfsp/gl}$ critically depends on the ASI value [molar $Al_2O_3/(Na_2O + K_2O + CaO - P_2O_5)$] of the melt because P becomes compatible in K-feldspar in high ASI melts (London, 1997). Thus relatively high P values in the inner cores of megacrysts DG-56 (Fig. 9a), DG-90 (Fig. 9b) and DG-177$_{(2)}$ (Fig. 9c) imply that magma recharge with silicic melts occurred during crystallization of the inner cores, when apatite was not in the liquidus assemblage and K-feldspar was the main reservoir for P. Conversely, the decrease of P in the outer core could point to a change in the granitic melt composition, possibly as a result of mixing.

A magma mixing hypothesis is strongly suggested by complex micro-textures, involving diverse accessory minerals [Th-rich monazite, monazite-(Ce), allanite and apatite] in the MC monzogranite (Dini *et al.*, 2004). These suggest complex reactions involving mixing between peraluminous (ASI > 1) and metaluminous (ASI < 1) melts (Dini *et al.*, 2004). Similar clusters (*c.* 150 μm) of micron-sized inclusions have been observed in megacryst DG-100$_{(2)}$ resembling the type-II texture (clusters of Th-rich monazite) described by Dini *et al.* (2004). During megacryst growth, recharge with mafic, P-rich, metaluminous melts (prior to resorption in most cases; see above) would decrease the ASI of the melt. As a consequence, $D(P)^{Kfsp/gl}$ decreases, thus explaining the drop of P content in the K-feldspar, without necessarily involving apatite crystallization.

The wide transitional zone (*c.* 2 mm) between the high and low P portions of megacryst DG-177$_{(2)}$ contrasts with much narrower zones in DG-56 and DG-90, which could reflect undercooling following the incorporation of these two megacrysts into MME (see above).

Li and Mg zoning: bearing on petrogenesis

Lithium (Li)

Li partitioning in peraluminous systems is mostly controlled by biotite crystallization [$D(Li)^{bt/melt}$ = 1–1·7,

Icenhower & London, 1995]. Biotite inclusions (in DG-44 and DG-90) display high Li content (739 ppm < Li < 1120 ppm; Electronic Appendix 5) compared with the host megacrysts (58 ppm < Li < 177 ppm; Table 2). We note that Li concentration in the MC K-feldspar is higher than previously reported for other plutons (Mason *et al.*, 1982, 1985; Smith & Brown, 1988).

Very little is known about Li partitioning in K-feldspar as the various influences of temperature, water activity and melt composition have not been examined experimentally. Our data suggest that the Li content decreases rimward, antithetically to Rb (Fig. 9). Low Li content at the rims of the megacrysts may be due to (1) mixing with a low-Li, mafic melt and/or (2) late input of a low-Li, high-Rb/Sr and high-Cs fluid in the magma system (see above) and/or (3) lower T and higher water activity during crystallization of the Kfm rims.

Magnesium (Mg)

Mg content varies from 14 to 27 ppm in pristine K-feldspar, and from 5 to 16 ppm in turbid zones (Table 2). Moreover, a crude correlation exists between Cs and Mg in turbid zones (not shown), suggesting that Mg abundance have also been affected by late-stage alteration as also suggested by Mason *et al.* (1985).

Calculated melt compositions [using a $D(\mathrm{Mg})^{\mathrm{fsp/melt}}$ value of 0·008; Mason *et al.*, 1982] range from *c.* 0·2 wt % to *c.* 0·5 wt % MgO, which is significantly lower than the average bulk-rock MgO content of the MC monzogranite and its MME (0·93% < MgO < 3·09%), but is within the range of leucogranitic and aplitic dykes cutting the pluton (<1%). This confirms the fact that megacrysts predominantly crystallized from strongly fractionated melts prior to K-feldspar crystallization, although the calculated melt composition remains largely speculative. In plagioclase feldspar, Mg partitioning is poorly correlated with variations in T and mol % An (e.g. Bindeman *et al.*, 1998). Similar partitioning behaviour for K-feldspar is expected. Thus Mg zoning could reflect changes in melt composition and/or water activity during megacryst growth.

The detailed profile

The higher spatial resolution afforded by the detailed profile across the resorption surface of megacryst DG-56 (Fig. 10) provides an opportunity to investigate a critical stage in the Kfm growth history in greater detail; that is, during recharge of the magma chamber with mafic magma.

The profile is divided into four zones (Fig. 14a), in which Ba and Sr are either positively [zones (1) and (3)] or negatively [zones (2) and (4)] correlated (Fig. 14a). Zone (4) is equivalent to the '0·2 mm zone' discussed above. When the Ba and Sr data from the detailed and core-to-rim profiles for megacryst DG-56 are combined, complex correlations emerge (Fig. 14b). In particular, the detailed traverse does not fall into the trend defined by the normal traverse (see Fig. 9a), but instead defines a loop towards high Sr concentrations followed by an increase in Ba as Sr declines towards the rim (Fig. 14b). This may reflect: (1) crystal fractionation (e.g. Long &

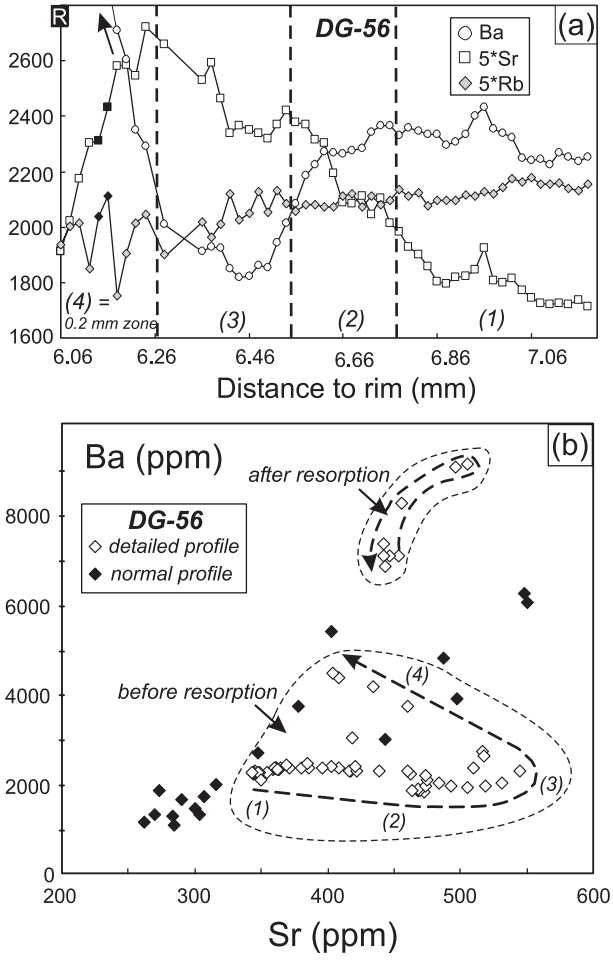

Fig. 14. (a) Ba and Sr (amplified five times) concentrations in the detailed profile of megacryst DG-56. The complex cross-overs displayed by Ba and Sr should be noted. Ba and Sr are positively correlated in zones (1) and (3) but negatively correlated in zones (2) and (4). Zone 4 is equivalent to the '0·2 mm zone' identified in Fig. 10. (b) Ba vs Sr covariation in megacryst DG-56 showing data from two SIMS profiles (Fig. 4). The megacryst cores and rims from the normal profile (filled symbols) define a mixing trend, which is scattered at intermediate values. The detailed profile across the resorption surface (open symbols, outlined by short dashed lines) defines a loop away from the main trend. This is best explained by non-equilibrium partitioning before and after resorption of the megacryst, as a result of the rise in temperature and faster diffusion of Sr than Ba in the melt, following an influx of hotter mafic magma. (See text for details.) Dashed arrows indicate the relative positions of the data points in the detailed profile in sequence towards the rim. Numerals (1–4) indicate the zones identified in (a).

Luth, 1986); (2) magma mixing between melts of contrasted composition (e.g. Blundy & Shimizu, 1991; Ginibre *et al.*, 2002); (3) changes in water activity (Long & Luth, 1986; Singer *et al.* 1995); (4) growth kinetics (e.g. Albarède & Bottinga, 1972).

Crystal fractionation?

Long & Luth (1986) have shown that normal and reverse Ba zoning in Kfm can be modelled by considering the simultaneous crystallization of other phases (quartz, plagioclase and a mafic phase). Crystal fractionation can also define curved evolutionary trends, such as observed in Fig. 14b. The abundance of Ba and Sr in the melt depends on the relative amount of K-feldspar (Ba and Sr compatible), biotite (Ba compatible) and plagioclase (± apatite) (Sr compatible) in the crystallizing assemblage. Following this hypothesis, increase of Sr and decrease of Ba from zone (1) to zone (3) (Fig. 14a) would imply that, in the host melt, the bulk D(Sr) is <1 whereas the bulk D(Ba) would still be >1. Using the partition coefficients of Icenhower & London (1995) for biotite, Icenhower & London (1996) for K-feldspar and Blundy & Wood (1991) for plagioclase, this situation can be modelled by crystallization of less than 12% of plagioclase + K-feldspar in a crystallizing assemblage mostly made of quartz and biotite. Modal analysis of Kfm indicates that biotite forms less than 12% of the inclusions (quartz, biotite, plagioclase; Fig. 5b), compared with more than 60% for plagioclase (Franzini *et al.*, 1974). Furthermore, no biotite- and/or quartz-rich trails are present in zones (2) and (3) of megacryst DG-56. Therefore, the modelled mineral assemblage can be ruled out.

Magma mixing?

Changes in trace element abundances in the outer core could reflect the growing influence of a mafic metaluminous melt, as discussed above. Although the Ba–Sr data from megacryst DG-56 define a mixing trend (Fig. 14b), the loop defined by the detailed profile (Fig. 14b) suggests that a third end-member may have been involved. This could reflect influx of a Ba-depleted silicic magma, as envisaged for the outer cores of megacrysts DG-90 and DG-177 (see above). However, we exclude this hypothesis because (1) the rimward increase of Sr (Fig. 14a) argues for a more mafic composition for the recharge magma and (2) the decrease of Ba in the detailed profile [i.e. the transition between zones (2) and (3)] occurs over a much shorter distance (*c.* 0·2 mm; Fig. 14b) than in megacrysts DG-90 (*c.* 1·2 mm; Fig. 9b) and DG-177$_{(2)}$ (*c.* 1·2 mm; Fig. 9c). Furthermore, a compositional break would be expected, but instead, there is a continuum in Ba, Rb and Sr concentrations from the outer core to the rim (see insets in Fig. 10). Therefore, complex short-term variations in the outer core cannot be explained only by magma mixing with another melt component.

Change in water activity?

Different H_2O content in the melt may potentially create Ba reverse zoning (Long & Luth, 1986). Thus an influx of hydrated magma may be responsible for the decrease of Ba from zone (1) to zone (3) (Fig. 14a). Although this hypothesis cannot be ruled out, it is doubtful that the complex co-variation of Ba and Sr (Fig. 14b) and continuous increase of Sr from zone (1) to zone (3) (Fig. 14b) could be explained solely by variable water activity in the melt.

Growth kinetics?

Several studies have demonstrated that departure from equilibrium can significantly affect trace element partitioning during crystal growth (e.g. Albarède & Bottinga, 1972; Allègre *et al.*, 1981; Shimizu, 1981; Loomis, 1982; Loomis & Welber, 1982; Singer *et al.*, 1995). Rapid growth, for example, may significantly influence the distribution of trace elements in plagioclase phenocrysts (Bottinga *et al.*, 1966; Loomis & Welber, 1982; Singer *et al.*, 1995; Ginibre *et al.*, 2002). Rapid growth limits diffusive equilibration between the boundary layer and the surrounding melt, hence depleting the boundary layer in compatible elements (Albarède & Bottinga, 1972). On the other hand, lower growth rates facilitate the incorporation of compatible elements, potentially creating reverse zoning (e.g. Lasaga, 1982). The cooling regime can also cause disequilibrium growth, since supersaturation at high degrees of undercooling may increase the incorporation of Ba into K-feldspar above the equilibrium amount (Morgan & London, 2003). As underlined by Magaritz & Hofmann (1978), kinetic effects may play an important role in granitic melts, where diffusion coefficients are likely to vary according to changes in temperature and/or H_2O content. Long (1978) investigated the influence of variable growth rate on element partitioning and noted a weak correlation for Ba, but none for Rb.

Because decoupling of Ba from Sr (Fig. 14a) cannot be explained by assuming equilibrium between melt and crystal, we suggest that disequilibrium growth must have occurred. Disequilibrium partitioning may be explained by different desorption–adsorption kinetics (Shimizu, 1981) between Ba and Sr. Briefly, different desorption energy quantifies the degree of attraction between the protosite and a given element and is controlled by the Coulomb attraction (Shimizu, 1981). Ba and Sr are both divalent, but Sr has a smaller ionic radius, which would suggest that Sr should be adsorbed more easily that Ba (higher z/r^2 for Sr; Shimizu, 1981). Therefore, the excursion towards high Sr content

displayed by the detailed profile (Fig. 14b) may reflect a higher degree of adsorption for Sr than for Ba, despite the latter having a higher crystal–melt partition coefficient.

However, the behaviour of other trace elements, such as Rb, argues against this mechanism. Within zones (1)–(3), Rb is anti-correlated with Sr although its concentration oscillates wildly in zone (4), when Sr decreases (Fig. 14a). The Rb ion has a single charge and larger ionic radius than both Ba and Sr and thus is less likely to adsorb onto the K-feldspar surface. If desorption–adsorption kinetics were responsible for trace element partitioning during disequilibrium growth, a marked decoupling between Rb and Ba and between Rb and Sr should be observed. However, the exact opposite is observed. Prior to resorption (Fig. 14b), Rb and Sr are reasonably well anti-correlated ($r^2 = 0{\cdot}51$) in the detailed profile, whereas Rb and Ba are less correlated ($r^2 = 0{\cdot}12$). This suggests that that disequilibrium partitioning mostly affects Ba, which cannot be adequately explained by differences in adsorption–desorption rates.

An alternative explanation may be to consider the effect of variations in the diffusion rate in granitic melts. Although competing for the same crystallographic M site, Ba and Sr have different diffusivities in both dry and wet granitic melts (i.e. Sr diffuses faster; Magaritz & Hofmann, 1978; Mungall *et al.*, 1999). A rise in temperature, caused by recharge with a mafic magma, would favour more rapid diffusion in the melt (Watson, 1982) and a decrease in the growth rate. High Ba in the melt expands the stability field of K-feldspar at high temperatures (up to 850°C; Morgan & London, 2003), therefore retarding its dissolution. Owing to its faster diffusivity in the melt, Sr would first be favoured at the crystal–melt interface and an increase of Sr would be expected [i.e. increase of $D(\mathrm{Sr})^{\mathrm{Fsp/gl}}$ and decrease of $D(\mathrm{Ba})^{\mathrm{Fsp/gl}}$ from zone (1) to zone (3); Fig. 14a]. However, rising temperature (prior to resorption) would gradually favour the incorporation of Ba at the expense of Sr [i.e. zone (3) to zone (4); Fig. 14a], producing a diffusion-like pattern (Figs 10 and 14a).

Rb diffuses at similar rate to Sr whereas Ba is slower in both natural obsidian (Jambon, 1982) and liquid diffusion experiments (Mungall *et al.*, 1999), in agreement with the observed pattern (Fig. 14a) as Ba is clearly decoupled from both Rb and Sr. In contrast to Sr, however, Rb displays a more erratic zoning pattern, becoming more 'noisy' rimwards within the outer core (Figs 10 and 14a), which may imply that the diffusion boundary layer was thinner (because of rising temperature) and responded more rapidly to external perturbations caused by the influx of mafic magma.

The relative enrichment of Ba compared with Sr after resorption (Fig. 14b) is also a non-equilibrium process involving the preferential incorporation of Ba (owing to its higher partition coefficient; Icenhower & London, 1996), sluggish diffusion at the melt–crystal interface and the incoming Ba-rich melt component. The Ba-rich zone corresponds to the 10–50 μm fringe of K-feldspar rimward of the resorption surfaces (Fig. 7b), which has also been reproduced experimentally (Wark & Stimac, 1992). After dissolution, megacryst DG-56 grew close to equilibrium conditions in a melt enriched in Ba and Sr in a zone-refining-like process. Abundant plagioclase inclusions rimward of resorption surfaces may indicate that megacryst growth was slower than prior to resorption.

Further evidence of disequilibrium growth is provided by the outermost rims of DG-44, which display a marked increase of mol % Or and decrease of Ba (Fig. 8a), as well as high Rb, B and Cs (Fig. 9d; Electronic Appendix 5). This is to be expected in the case of rapid growth (Singer *et al.*, 1995), as rapid growth depletes the diffusion boundary layer in compatible elements (Albarède & Bottinga, 1972; Singer *et al.*, 1995). Rapid growth is associated with an undercooling event that could have occurred during (1) emplacement of the pluton into 'cold' country rocks, and/or (2) devolatilization.

These observations show that the common assumption that growth rates in granitic melts (*sensu lato*) are low enough to preclude departure from equilibrium conditions (e.g. Long & Luth, 1986; Blundy & Shimizu, 1991) needs to be revised. Kinetic effects and non-equilibrium processes may play an important role during trace element partitioning in plutonic rocks, which would be enhanced during periods of thermal disturbance, during magma recharge (i.e. the outer cores) and/or magma emplacement (i.e. the outer rim).

PETROGENETIC MODEL

K-feldspar megacrysts record various stages of magmatic evolution, presumably in a magma chamber subject to open-system processes (e.g. Zorpi *et al.*, 1989; Metcalf *et al.*, 1995; Fig. 15). This assumption is largely based on multiple evidence of magma mixing or mingling (MME) and the abundant crustal xenoliths, distinct from the country rock, that occur throughout the MC intrusion (Fig. 2). An important feature that needs to be taken into account is that the three facies (San Piero, San Francesca and Sant' Andrea; Fig. 2) have similar Sr and Nd isotopic compositions (Dini *et al.*, 2002), despite marked chemical differences (Dini *et al.*, 2004). It is suggested that these facies correspond to the original architecture of the granitic magma chamber.

As pointed out above, it is important to note that the petrogenetic history retrieved by the megacryst zoning reflects both time and space. Thus the model presented below (Fig. 15) is, in essence, oversimplified because overlaps of petrogenetic processes are inevitable.

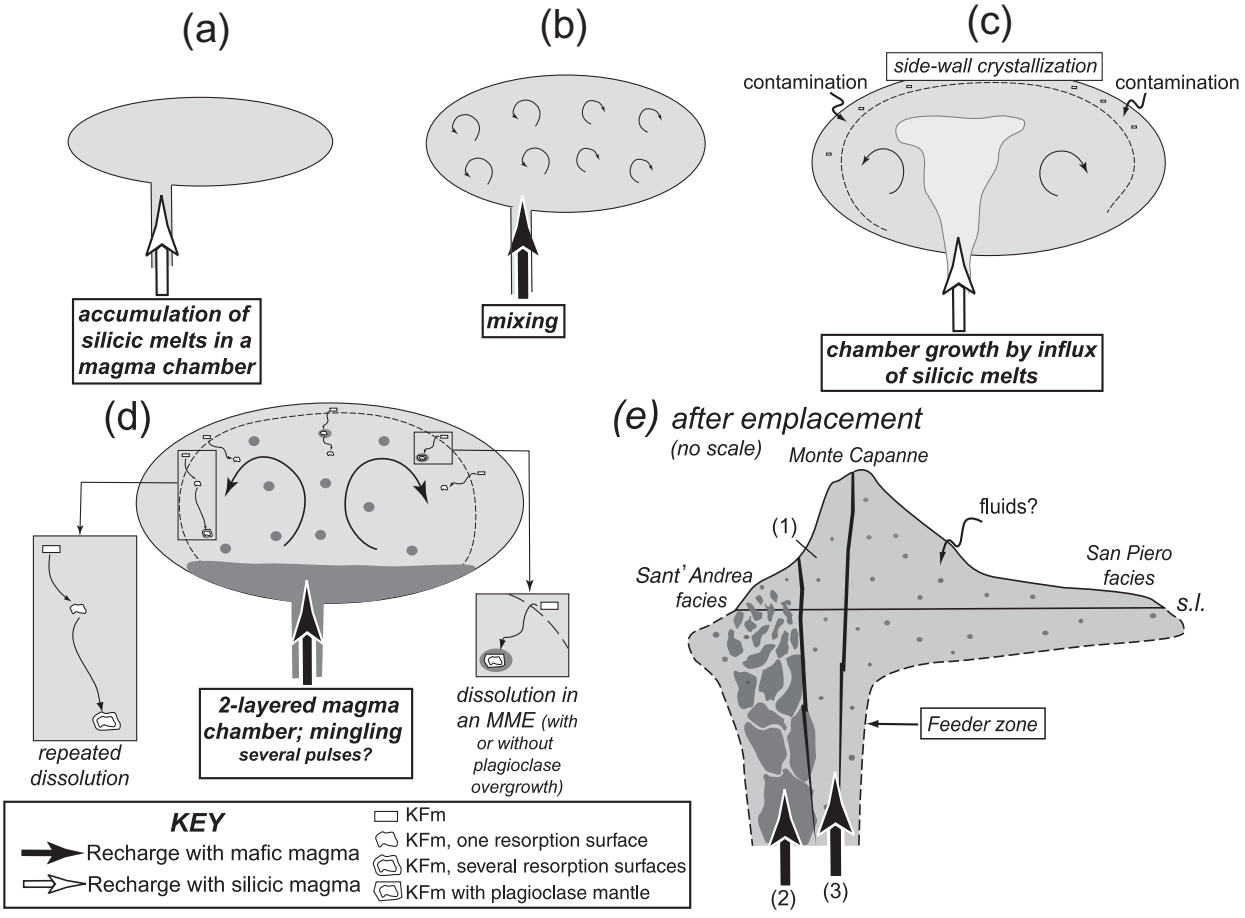

Fig. 15. Model for the evolution of the Monte Capanne plutonic system. (a) Accumulation of silicic (anatectic) melts in a magma chamber (whose shape is speculative). (b) Early hybridization between anatectic and mantle-derived melts was favoured because of low crystal content and small compositional contrast in a turbulent environment. (c) Side-wall interplay between crustal contamination, crystallization and magma recharge with differentiated magmas during growth of the magma chamber. (d) Influx of mafic magma in the chamber followed by crystal fractionation and mingling, leading to the formation of blobs of hybrid magma (MME), further dispersed by convection. Dissolution occurs either in MME (with or without plagioclase overgrowth) or in response to rising temperature, possibly in deeper parts of the magma chamber. (e) Final stage of the pluton after its emplacement, which occurred through feeder dykes with successive batches of hybrid magma (from the San Piero to the Sant' Andrea facies) (1), later intruded by a batch of evolved mafic magma (2), possibly coming from the bottom of the chamber. Post-plutonic leucogranite (not shown) and Orano dykes (in black, 3) represent the last magmatic products of the MC plutonic system. Hydrothermal fluids may be responsible for higher I_{Sr} at the outer rim of some megacrysts. s.l., sea level.

However, the model accounts for most of the chemical and isotopic zoning in the Kfm, as well as field observations, whole-rock data and mineral data (Dini *et al.*, 2002, 2004; Gagnevin *et al.*, 2004).

(1) Large-scale anatexis of the Tuscan Palaeozoic basement led to the formation of a large volume of peraluminous magma (Dupuy & Allègre, 1972; Taylor & Turi, 1976; Giraud *et al.*, 1986; Poli *et al.*, 1989), which accumulated in a magma chamber (Fig. 15a). The crustal magma involved in the genesis of the MC pluton is inferred to be similar to the leucocratic facies from Giglio Island (Poli, 1992) or the Cotoncello dyke in Elba (Fig. 11b; Dini *et al.*, 2002).

(2) Hybridization affected the MC pluton early in its crystallization history (Fig. 15b). The felsic magma contained plagioclase and biotite as main phases. The presence of similar patchy-zoned plagioclase phenocryst cores and Ca-rich corroded plagioclase (up to 79 mol % An) scattered in both the mafic enclaves and the monzogranite (Barbarin, 1990; Gagnevin *et al.*, 2004), as well as reaction micro-textures between early-formed accessory minerals (monazite, allanite and apatite) (Dini *et al.*, 2004), both provide evidence for early hybridization between mafic and silicic magmas (Fig. 15b). Mechanical, and perhaps chemical, mixing may have been favoured because of the evolved andesitic character (Sparks & Marshall, 1986) and high water content (Frost & Mahood, 1987; Neves & Vauchez, 1995) of the mafic magma, possibly represented by Si-rich (SiO_2 >59%) high-K andesites on Capraia (Fig. 1).

(3) Extensive fractionation of plagioclase, biotite, quartz and K-feldspar occurred in the felsic magma chamber, as suggested by the fractionated trace element signature in the core region (low Ba, Sr, Mg) of the Kfm. This could have occurred along wall-rock zones through sidewall crystallization in a boundary layer (e.g. Sawka *et al.*, 1990; Mahood *et al.*, 1996; Fig. 15c), where fractionated melts accumulated at the top of the magma chamber (Sawka *et al.*, 1990; Verplanck *et al.*, 1999).

(4) Variably high I_{Sr} values in the megacryst inner cores (Fig. 11) suggest that crystal fractionation was accompanied by wall-rock contamination (Fig. 15c), as indicated by digested crustal xenoliths and whole-rock Sr and Nd isotopic data (Gagnevin *et al.*, 2004).

(5) The magma chamber was further refilled with silicic (i.e. no resorption in the inner core region; Fig. 11a and f) and differentiated (i.e. flat Ba zoning patterns in the inner core of DG-90; Fig. 9b) magma, possibly coming from deeper levels of magma storage (Fig. 15c). Because of its lower density, it is possible that the silicic recharge magma may have risen to higher levels in the magma chamber (Fig. 15c).

(6) The occurrence of resorption surfaces in the rim region of the megacrysts (Fig. 5b) strongly suggests that recharge with mafic magma subsequently occurred (Fig. 15d). Because of the high degree of crystallinity of the felsic magma, a two-layered magma chamber may have formed. After ponding of the mafic magma at the base of the magma chamber (Fig. 15d) (Wiebe, 1993; Wiebe *et al.*, 1997), crystal fractionation in the mafic magma (Bateman, 1995) was associated with mingling of residual melts as thermal equilibrium was attained (Castro *et al.*, 1990; Poli & Tommasini, 1991), forming a double-diffusive layer of hybrid magma, whose composition would be similar to that of the MME. Recharge would have triggered large convective instabilities (Wiebe *et al.*, 1997; Fig. 15d), contributing to the dispersal of blobs of hybrid magma in the overlying monzogranitic magma and recycling of K-feldspar megacrysts (e.g. Blundy & Shimizu, 1991; Fig. 15d). Resorption of zoned Kfm may have occurred (1) in MME (with or without plagioclase overgrowth; Fig. 15d) or (2) during prolonged residence in hybrid Ba- and Sr-rich melts in the lower part of the magma chamber, in response to repeated recharge with mafic magmas (Fig. 15d). We emphasize that a wide variety of dissolution environments are likely to have been involved, especially in megacrysts that exhibit several resorption surfaces.

(7) It is possible that influx of mafic magma may have triggered incremental pluton emplacement (Zorpi *et al.*, 1989), as an influx of mafic magma would trigger eruption from a shallow magma chamber (Sparks *et al.*, 1977). Feeder dykes (such as the Cotoncello dyke; Dini *et al.*, 2002) preserve evidence for magma transport at shallow crustal levels (<1 kbar). Bouillin *et al.* (1993) interpreted AMS patterns in the NW part of the pluton (Sant' Andrea facies; Fig. 2) to represent a feeder zone (Fig. 15e). The Sant' Andrea facies is characterized by a large volume of evolved (granodioritic), hybrid, sometimes composite, MME (Fig. 3b), suggesting renewed commingling after the final emplacement of the monzogranitic mass (Fig. 15e). This may represent another pulse of hybrid, relatively evolved magma into the enclave-bearing monzogranitic crystal mush, possibly via the injection of a large syn-plutonic dyke (Fig. 15e), which is likely to have come from lower, more mafic, parts of the magma chamber (i.e. Fig. 15d).

(8) Following renewed commingling in the Sant' Andrea facies (Fig. 2; possibly representing the lowest part of the intrusion), crystal fractionation was dominant in the San Francesco and San Piero facies (Fig. 2), as attested by abundant leucocratic dykes and veins in these two facies. It is argued that the chemical zonation of the intrusion, illustrated by the data of Dini *et al.* (2004), is inherited from this fractionation event.

(9) The last melt pockets possibly mixed with hydrothermal fluids (see above; Fig. 15e), as suggested by higher I_{Sr} at the rims of some Kfm (Fig. 11e and f).

(10) The hybrid Orano dykes were the last pulses of the MC plutonic system (Fig. 15e) and support the existence of a magma chamber at deeper levels.

CONCLUDING REMARKS

This study, combining major, trace element and Sr isotopic data from zoned K-feldspar megacrysts, provides insights into the complex multi-stage evolution of a plutonic system subject to open-system behaviour. This is suggested by mafic enclaves and metasedimentary xenoliths, which are good indicators of mafic–felsic interactions (e.g. Didier & Barbarin, 1991) and crustal contamination (e.g. Van Bergen & Barton, 1984), respectively.

K-feldspar megacrysts are a valuable tool to decipher the magmatic history. Through their internal morphology (i.e. occurrence of resorption surfaces), Kfm grains in the MC pluton provide a robust petrographic record of magma mixing. Despite protracted cooling and evidence of subsolidus alteration, these megacrysts preserve large primary Sr isotopic variations ($^{87}Sr/^{86}Sr_{(i)}$ decreases rimward) and marked trace element zoning (e.g. Ba, Sr, Rb, P) reflecting growth zoning rather than diffusive equilibration. This can be reconciled with a magma chamber model whereby different magma recharge events (silicic and mafic) contributed to the establishment of a zoned magma system, both at the whole-rock and mineral scale. Pb isotopic profiles (obtained by laser ablation MC-ICP-MS) obtained on the same megacrysts concur with this

model (Gagnevin *et al.*, 2005). In particular, the rims are characterized by high $^{208}Pb/^{206}Pb$ and $^{207}Pb/^{206}Pb$, which reflect the nature of the mantle-derived magma component involved in the mixing–mingling process (Gagnevin *et al.*, 2005).

Disequilibrium has occurred at different stages of megacryst growth; that is, during outer core and rim crystallization. This shows that care must be taken in interpreting the timescales calculated from trace element zoning (Zellmer *et al.*, 1999), especially when various magma recharge events are envisaged (Zellmer *et al.*, 2003).

ACKNOWLEDGEMENTS

We thank Michael Murphy and Richard Walshaw for providing assistance with TIMS isotopic analyses, and Tom Culligan for making thin-sections. Richard Hinton (Edinburgh) and Stuart Kearns (Bristol) are thanked for assistance with ion microprobe and electron microprobe analyses, respectively. We thank Bob Cliff for access to the microdrill at the University of Leeds. We are grateful to Franck Tepley, Ewa Slaby and, especially, Tod Waight for constructive and thorough reviews, and to Marjorie Wilson for editorial work and helpful comments on the original typescript, all of which led to improvements. We acknowledge the support of the European Community Access to Research Infrastructure action of the Improving Human Potential Programme, contract HPRI-CT-1999-00008 awarded to Professor B. J. Wood (EU Geochemical Facility, University of Bristol). This research was supported by an Enterprise Ireland grant (SC/1999/034), by EU contract EVG1-CT-2002-00058 awarded to J.S.D. and by research project COFIN-1999 awarded to G.P.

SUPPLEMENTARY DATA

Supplementary data for this paper are available on *Journal of Petrology* online.

REFERENCES

Albarède, F. & Bottinga, Y. (1972). Kinetic disequilibrium in trace element partitioning between phenocrysts and host lava. *Geochimica et Cosmochimica Acta* **36**, 141–156.

Aldighieri, B., Gamba, A., Groppelli, G., Malara, F., Pasquare, G., Testa, B. & Wijbrans, J. (1998). Methodology for the space–time definition of lateral collapse: the evolution model of Capraia Island (Italy). *Proceedings of International Association for Mathematical Geology* 79–85.

Allègre, C. J., Provost, A. & Jaupart, C. (1981). Oscillatory zoning: a pathological case of crystal growth. *Nature* **294**, 223–228.

Anderson, A. T., Davis, A. M. & Lu, F. (2000). Evolution of Bishop tuff rhyolitic magma based on melt and magnetite inclusions and zoned phenocrysts. *Journal of Petrology* **41**, 449–473.

Andersson, U. B. & Eklund, O. (1994). Cellular plagioclase intergrowths as a result of crystal–magma mixing in the Proterozoic Aland rapakivi batholith, SW Finland. *Contributions to Mineralogy and Petrology* **117**, 124–136.

Bacon, C. R. (1989). Crystallisation of accessory phases in magmas by local saturation adjacent to phenocrysts. *Geochimica et Cosmochimica Acta* **53**, 1055–1066.

Bagnoli, G., Gianelli, G., Puxeddu, M., Rau, A., Squarci, P. & Tongiorgi, M. (1979). A tentative stratigraphic reconstruction of the Tuscan Paleozoic basement. *Memoria della Società Geologica Italiana* **20**, 99–116.

Barbarin, B. (1990). Plagioclase xenocrysts and mafic magmatic enclaves in some granitoids of the Sierra Nevada batholith, California. *Journal of Geophysical Research* **95**, 17747–17756.

Bateman, R. (1995). The interplay between crystallization, replenishment and hybridization in large felsic magma chambers. *Earth-Science Reviews* **39**, 91–106.

Bindeman, I. N., Davis, A. M. & Drake, M. J. (1998). Ion microprobe study of plagioclase–basalt partition coefficients at natural concentration level of trace elements. *Geochimica et Cosmochimica Acta* **62**, 1175–1193.

Blundy, J. D. & Shimizu, N. (1991). Trace element evidence for plagioclase recycling in calc-alkaline magmas. *Earth and Planetary Science Letters* **102**, 178–197.

Blundy, J. D. & Wood, B. J. (1991). Crystal-chemical controls on the partitioning of Sr and Ba between plagioclase feldspar, silicate melts, and hydrothermal solution. *Geochimica et Cosmochimica Acta* **55**, 193–209.

Bottinga, Y., Kudo, A. & Weill, D. (1966). Some observation on oscillatory zoning and crystallisation of magmatic plagioclase. *American Mineralogist* **51**, 792–806.

Bouillin, J. P., Bouchez, J. L., Lespinasse, P. & Pecher, A. (1993). Granite emplacement in an extensional setting: an AMS study of the magmatic structures of Monte Capanne (Elba, Italy). *Earth and Planetary Science Letters* **118**, 263–279.

Brophy, J. G., Dorais, M. J., Donnelly-Nolan, J. & Singer, B. S. (1996). Plagioclase zonation styles in hornblende gabbro inclusions from Little Glass Mountain, Medicine Lake volcano, California: implications for fractionation mechanisms and the formation of compositional gaps. *Contributions to Mineralogy and Petrology* **126**, 121–136.

Bussy, F. (1990*a*). Petrogénèse des enclaves microgrenues associées aux granitoides calco-alcalins: exemples des massifs varisques du Mont-Blanc (Alpes occidentales) et Miocène du Monte Capanne (Ile d'Elbe, Italie). *Mémoire de Géologie, Lausanne* **7**, 309 pp.

Bussy, F. (1990*b*). The rapakivi texture of feldspars in a plutonic mixing environment: a dissolution–recrystallisation process? *Geological Journal* **25**, 319–324.

Bussy, F. (1991). Enclaves of the late Miocene Monte Capanne granite, Elba Island, Italy. In: Didier, J. & Barbarin, B. (ed.) *Enclaves and Granite Petrology. Development in Petrology* **13**, 167–178.

Carron, J. P. & Lagache, M. (1982). Zonation des elements en traces au cours de la croissance de cristaux dans les bains silicates: l'exemple de Rb, Cs, Sr et Ba dans le système Qz–Ab–Or–H_2O. *Geochimica et Cosmochimica Acta* **46**, 2151–2158.

Castro, A., De La Rosa, J. D. & Stephens, W. E. (1990). Magma mixing in the subvolcanic environment: petrology of the Gerena interaction zone near Seville, Spain. *Contributions to Mineralogy and Petrology* **105**, 9–26.

Chappell, B. W., White, A. J. R. & Wyborn, D. (1987). The importance of residual source material (restite) in granite petrogenesis. *Journal of Petrology* **28**, 1111–1138.

Cherniak, D. J. (1996). Strontium diffusion in sanidine and albite, and general comments on strontium diffusion in alkali feldspars. *Geochimica et Cosmochimica Acta* **60**, 5037–5043.

Cherniak, D. J. (2002). Ba diffusion in feldspar. *Geochimica et Cosmochimica Acta* **66**, 1641–1650.

Conticelli, S., Manetti, P. & Menichetti, S. (1992). Mineralogy, geochemistry and Sr-isotopes in orendites from South Tuscany, Italy: constraints on their genesis and evolution. *European Journal of Mineralogy* **4**, 1359–1375.

Conticelli, S., D'Antonio, M., Pinarelli, L. & Civetta, L. (2002). Source contamination and mantle heterogeneity in the genesis of Italian potassic and ultrapotassic volcanic rocks: Sr–Nd–Pb isotope data from Roman Province and Southern Tuscany. *Mineralogy and Petrology* **74**, 189–222.

Cox, R. A., Dempster, T. J., Bell, B. R. & Rogers, G. (1996). Crystallisation of the Shap Granite: evidence from zoned K-feldspar megacrysts. *Journal of the Geological Society, London* **153**, 625–635.

Crank, J. (1975). *The Mathematics of Diffusion*, 2nd edn. Oxford: Clarendon Press.

Daly, J. S. & Poli, G. (1999). Petrogenetic insights from microchemical investigations of magmatic K-feldspars in the 7 Ma Elba monzogranite. *Irish Journal of Earth Science* **17**, 128.

Davidson, J. P. & Tepley, F. J., III (1997). Recharge in volcanic systems: evidence from isotope profiles of phenocrysts. *Science* **275**, 826–829.

Davidson, J. P., De Silva, S. L., Holden, P. & Halliday, A. N. (1990). Small-scale disequilibrium in a magmatic inclusion and its more silicic host. *Journal of Geophysical Research* **95**, 17661–17675.

Davidson, J. P., Tepley, F. J., III & Knesel, K. M. (1998). Isotopic fingerprinting may provide insights into evolution of magmatic systems. *EOS Transactions, American Geophysical Union* **17/15**, 185–193.

Davidson, J. P., Tepley, F., III, Palacz, Z. & Meffan-Main, S. (2001). Magma recharge, contamination and residence times revealed by *in situ* laser ablation isotopic analysis of feldspar in volcanic rocks. *Earth and Planetary Science Letters* **184**, 427–442.

Davies, G. R., Halliday, A. N., Mahood, G. A. & Hall, C. A. (1994). Isotopic constraints on the production rates, crystallisation histories and residence times of pre-caldera silicic magmas, Long Valley, California. *Earth and Planetary Science Letters* **125**, 17–37.

Didier, J. (1973). *Granites and their Enclaves: the Bearing of Enclaves on the Origin of Granites. Development in Petrology* **3**, 393 pp.

Didier, J. & Barbarin, B. (1991). *Enclaves and Granite Petrology. Development in Petrology* **13**, 625 pp.

Dini, A., Innocenti, F., Rocchi, S., Tonarini, S. & Westerman, D. S. (2002). The magmatic evolution of the late Miocene laccolith–pluton–dyke granitic complex of Elba Island, Italy. *Geological Magazine* **139**, 257–279.

Dini, A., Rocchi, S. & Westerman, D. S. (2004). Reaction microtextures of REE–Y–Th–U accessory minerals in the Monte Capanne pluton (Elba Island, Italy): a possible indicator of hybridisation processes. *Lithos* **78**, 101–118.

Dupuy, C. & Allègre, C. J. (1972). Fractionnement K/Rb dans les suites ignimbritiques Toscane. Un exemple de rejuvenation crustale. *Geochimica et Cosmochimica Acta* **36**, 437–458.

Elburg, M. A. (1996). Evidence of isotopic equilibration between microgranitoid enclaves and host granodiorite, Warburton Granodiorite, Lachlan Fold Belt, Australia. *Lithos* **38**, 1–22.

Feldstein, S. N., Halliday, A. N., Davies, G. R. & Hall, C. M. (1994). Isotope and microsampling: constraints on the history of an S-type rhyolite, San Vincenzo, Tuscany, Italy. *Geochimica et Cosmochimica Acta* **58**, 943–958.

Ferrara, G. & Tonarini, S. (1985). Radiometric geochronology in Tuscany: results and problems. *Rendiconti della Società Italiana di Mineralogia e Petrologia* **40**, 111–124.

Ferrara, G., Giuliani, O., Tonarini, S. & Villa, I. M. (1988). Datability and isotopic disequilibrium in anatectic volcanites from San Vincenzo and Tolfa (Tuscany–Latium). *Rendicondi della Società Italiana di Mineralogia e Petrologia* **7**, 72.

Ferrara, G., Petrini, R., Serri, G. & Tonarini, S. (1989). Petrology and isotope-geochemistry of San Vincenzo rhyolites (Tuscany, Italy). *Bulletin of Volcanology* **51**, 379–388.

Ferrari, L., Conticelli, S., Burlamacchi, L. & Manetti, P. (1996). Volcanological evolution of the Monte Amiata, Southern Tuscany: new geological and petrochemical data. *Acta Vulcanologica* **8**, 41–56.

Franzini, M. & Leoni, L. (1974). Synneusis of plagioclase with K-feldspar in the Monte Capanne (Elba Island) granodiorite. *Rendicondi della Società Italiana di Mineralogia e Petrologia* **30**, 21–30.

Franzini, M., Leoni, L. & Orlandi, P. (1974). Mineralogical and geochemical study of K-feldspar megacrysts from the Elba (Italy) granodiorite. *Atti della Società Toscana di Scienze Naturale, Memorie* **A81**, 356–378.

Frost, T. P. & Mahood, G. A. (1987). Field, chemical, and physical constraints on mafic–felsic magma interaction in the Lamarck Granodiorite, Sierra Nevada, California. *Geological Society of America Bulletin* **99**, 272–291.

Gagnevin, D., Daly, J. S. & Poli, G. (2001). Mineral-scale investigation of the petrogenesis of the 7 Ma old Monte Capanne pluton (Elba Island, Tuscany, Italy). *Journal of Conference Abstracts* **6**(1), 572.

Gagnevin, D., Daly, J. S. & Poli, G. (2004). Petrographic, geochemical and isotopic constraints on magma dynamics and mixing in the Miocene Monte Capanne monzogranite (Elba Island, Italy). *Lithos* **78**, 157–195.

Gagnevin, D., Daly, J. S., Waight, T., Morgan, D. & Poli, G. (2005). Pb isotopic zoning of K-feldspar megacrysts determined by laser ablation multiple-collector ICP-MS: insights into granite petrogenesis. *Geochimica et Cosmochimica Acta* **69**, 1899–1915.

Giletti, B. J. (1991). Rb and Sr diffusion in alkali feldspars, with implications for cooling histories of rocks. *Geochimica et Cosmochimica Acta* **55**, 1331–1343.

Ginibre, C., Wörner, G. & Kronz, A. (2002). Minor- and trace-element zoning in plagioclase: implications for magma chamber processes at Parinatoca volcano, northern Chile. *Contributions to Mineralogy and Petrology* **143**, 300–315.

Ginibre, C., Wörner, G. & Kronz, A. (2004). Structure and dynamics of the Laacher See magma chamber (Eifel, Germany) from major and trace element zoning in sanidine: a cathodoluminescence and electron microprobe study. *Journal of Petrology* **45**, 2197–2223.

Giraud, A., Dupuy, C. & Dostal, J. (1986). Behaviour of trace elements during magmatic processes in the crust: application to acidic volcanic rocks of Tuscany (Italy). *Chemical Geology* **57**, 269–288.

Glazner, A. F., Ussier, W., III & Mies, J. W. (1988). Fate of granitic minerals in mafic magmas. *EOS Transactions, American Geophysical Union* **69**, 1504.

Guo, J. & Green, T. H. (1989). Barium partitioning between alkali feldspar and silicate liquid at high temperature and pressure. *Contributions to Mineralogy and Petrology* **102**, 328–335.

Halama, R., Waight, T. & Markl, G. (2002). Geochemical and isotopic zoning patterns of plagioclase megacrysts in gabbroic dykes from the Gardar Province, South Greenland: implications for crystallisation processes in anorthositic magmas. *Contributions to Mineralogy and Petrology* **144**, 109–127.

Hall, A., Bencini, A. & Poli, G. (1991). Magmatic and hydrothermal ammonium in granites of the Tuscan Magmatic Province, Italy. *Geochimica et Cosmochimica Acta* **55**, 3657–3664.

Halliday, A. N., Davidson, J. P., Hildreth, W. & Holden, P. (1991). Modelling the petrogenesis of high Rb/Sr silicic magma. *Chemical Geology* **92**, 107–114.

Harris, N., Vance, D. & Ayres, M. (2000). From sediment to granite: timescales of anatexis in the upper crust. *Chemical Geology* **162**, 155–167.

Hervig, R. L. & Dunbar, N. W. (1992). Cause of chemical zoning in the Bishop (California) and Bandelier (New Mexico) magma chambers. *Earth and Planetary Science Letters* **111**, 97–108.

Hibbard, M. J. (1965). Origin of some alkali feldspar phenocrysts and their bearing on petrogenesis. *American Journal of Science* **263**, 245–261.

Hibbard, M. J. (1981). The magma mixing origin of mantled feldspars. *Contributions to Mineralogy and Petrology* **76**, 158–170.

Hinton, R. (1995). Ion microprobe analysis in geology. In: Potts, P. J., Bowles, J. F. W., Reed, S. J. B. & Cave, M. R. (eds) *Microprobe Techniques in the Earth-Sciences*. London: Chapman and Hall, pp. 235–289.

Icenhower, J. & London, D. (1995). An experimental study of element partitioning among biotite, muscovite, and coexisting peraluminous silicic melt at 200 MPa (H_2O). *American Mineralogist* **80**, 1229–1251.

Icenhower, J. & London, D. (1996). Element partitioning of Rb, Cs, Sr and Ba between alkali feldspar and peraluminous melt. *American Mineralogist* **81**, 719–734.

Innocenti, F., Serri, G., Ferrara, G., Manetti, P. & Tonarini, S. (1992). Genesis and classification of the rocks of the Tuscan Magmatic Province: thirty years after Marinelli's model. *Acta Vulcanologica* **2**, 247–265.

Innocenti, F., Westerman, D. S., Rocchi, S. & Tonarini, S. (1997). The Montecristo monzogranite (Northern Tyrrhenian Sea, Italy): a collisional pluton in an extensional setting. *Geological Journal* **32**, 131–151.

Irving, A. J. & Frey, F. A. (1984). Trace elements abundances in megacrysts and their host basalts: constraints on partition coefficients and megacryst genesis. *Geochimica et Cosmochimica Acta* **48**, 1201–1221.

Jolivet, L., Faccenna, C., Goffe, B., Mattei, M., Rossetti, F., Brunet, C., Storti, F., Funicielli, R., Cadet, J. P., d'Agostino, N. & Parra, T. (1998). Midcrustal shear zone in postorogenic extension: example from the northern Tyrrhenian Sea. *Journal of Geophysical Research* **103**, 12123–12160.

Juteau, M., Michard, A. J. & Albarède, F. (1984). Isotopic heterogeneities in the granitic intrusion of Monte Capanne (Elba Island, Italy) and dating concepts. *Journal of Petrology* **25**, 532–545.

Keller, J. V. A. & Pialli, G. (1990). Tectonics of the Island of Elba: a reappraisal. *Bolletino della Società Geologica Italiana* **109**, 413–425.

Knesel, K. M., Davidson, J. P. & Wendell, A. D. (1999). Evolution of silicic magma through assimilation and subsequent recharge: evidence from Sr isotopes in sanidine phenocrysts, Taylor Creek Rhyolite, NM. *Journal of Petrology* **40**, 773–786.

Lasaga, A. C. (1982). Towards a master equation in crystal growth. *American Journal of Science* **282**, 1264–1288.

Lee, M. R., Waldron, K. A. & Parsons, I. (1995). Exsolution and alteration microtextures in alkali feldspar phenocrysts from the Shap granite. *Mineralogical Magazine* **59**, 63–78.

Leeman, W. P. & Phelps, D. W. (1981). Partitioning of rare earth and other trace elements between sanidine and coexisting volcanic glass. *Journal of Geophysical Research* **86**, 10193–10199.

Lesher, C. E. (1994). Kinetics of Sr and Nd exchange in silicate liquids: theory, experiments, and applications to uphill diffusion, isotopic equilibration, and irreversible mixing of magmas. *Journal of Geophysical Research* **99**, 9585–9604.

London, D. (1997). Estimating abundances of volatile and other mobile components in evolved silicic melts through mineral–melt equilibria. *Journal of Petrology* **38**, 1691–1706.

Long, P. E. (1978). Experimental determination of partition coefficients for Rb, Sr, and Ba between alkali feldspar and silicate liquid. *Geochimica et Cosmochimica Acta* **42**, 833–846.

Long, P. E. & Luth, W. C. (1986). Origin of K-feldspar megacrysts in granitic rocks: implications of a partitioning model for barium. *American Mineralogist* **71**, 367–375.

Loomis, T. P. (1982). Numerical simulations of crystallisation processes of plagioclase in complex melts: the origin of major and oscillatory zoning in plagioclase. *Contributions to Mineralogy and Petrology* **81**, 219–229.

Loomis, T. P. & Welber, P. W. (1982). Crystallisation processes in the Rocky Hill granodiorite pluton, California: an interpretation based on compositional zoning of plagioclase. *Contributions to Mineralogy and Petrology* **81**, 230–239.

Maas, R., Nicholls, I. A., Greig, A. & Nemchin, A. (2001). U–Pb zircon studies of mid-crustal metasedimentary enclaves from the S-type Deddick granodiorite, Lachlan Fold Belt, SE Australia. *Journal of Petrology* **42**, 1429–1448.

Maas, R., Nicholls, I. A. & Legg, C. (1997). Igneous and metamorphic enclaves in the S-type Deddick Granodiorite, Lachlan Fold Belt, SE Australia: petrographic, geochemical and Nd–Sr isotopic evidence for crustal melting and magma mixing. *Journal of Petrology* **38**, 815–841.

Magaritz, M. & Hofmann, A. W. (1978). Diffusion of Sr, Ba and Na in obsidian. *Geochimica et Cosmochimica Acta* **42**, 595–605.

Mahood, G. A., Nibler, G. E. & Halliday, A. N. (1996). Zoning patterns and petrologic processes in peraluminous magma chamber: Hall Canyon pluton, Panamint Mountains, California. *Geological Society of America Bulletin* **108**, 437–453.

Mason, R. A., Smith, J. W., Dawson, J. B. & Treves, S. B. (1982). A reconnaissance of trace elements in anorthoclase megacrysts. *Mineralogical Magazine* **46**, 7–11.

Mason, R. A., Parsons, I. & Long, J. V. P. (1985). Trace and minor element chemistry of alkali feldspars in the Klokken Layered Syenite Series. *Journal of Petrology* **26**, 952–970.

Maury, R. C. & Didier, J. (1991). Xenoliths and the role of assimilation. In: Didier, J. & Barbarin, B. (eds) *Enclaves and Granite Petrology. Development in Petrology* **13**, 529–542.

Mehnert, K. R. & Büsch, W. (1981). The Ba content of K-feldspar megacrysts in granite: a criterion for their formation. *Neues Jahrbüch für Mineralogie, Abhandlungen* **140**, 221–252.

Metcalf, R. V., Smith, E. I., Walker, J. D., Reed, R. C. & Gonzales, D. A. (1995). Isotopic disequilibrium among commingled hybrid magmas: evidence for a two-stage magma mixing–commingling process in the Mt. Perkins pluton, Arizona. *Journal of Geology* **103**, 509–527.

Montel, J.-M., Didier, J. & Pichavant, M. (1991). Origin of surmicaceous enclaves in intrusive granites. In: Didier, J. & Barbarin, B. (eds) *Enclaves and Granite Petrology. Development in Petrology* **13**, 509–528.

Morgan, G. B., VI & London, D. (2003). Trace-element partitioning at conditions far from equilibrium: Ba and Cs distributions between alkali feldspar and undercooled hydrous granitic liquid at 200 MPa. *Contributions to Mineralogy and Petrology* **144**, 722–738.

Mungall, J. E., Dingwell, D. B. & Chaussidon, M. (1999). Chemical diffusivities of 18 trace elements in granitoid melts. *Geochimica et Cosmochimica Acta* **63**, 2599–2610.

Nash, W. P. & Crecraft, H. R. (1985). Partition coefficients for trace elements in silicic magmas. *Geochimica et Cosmochimica Acta* **49**, 2309–2322.

Neves, S. P. & Vauchez, A. (1995). Successive mixing and mingling of magmas in a plutonic complex of Northeast Brazil. *Lithos* **34**, 275–299.

Nitoi, E., Munteanu, M., Marincea, S. & Paraschivoiu, V. (2002). Magma–enclave interactions in the East Carpathian Subvolcanic Zone, Romania: petrogenetic implications. *Journal of Volcanology and Geothermal Research* **118**, 229–259.

Peccerillo, A. (1999). Multiple mantle metasomatism in central–southern Italy: geochemical effects, timing and geodynamic implications. *Geology* **27**, 315–318.

Peccerillo, A., Poli, G. & Serri, G. (1988). Petrogenesis of orenditic and kamafugitic rocks from Central Italy. *Canadian Mineralogist* **26**, 45–65.

Peccerillo, A., Poli, G. & Donati, C. (2001). The Plio-Quaternary magmatism of southern Tuscany and northern Latium: compositional characteristics, genesis and geodynamic significance. *Ofioliti* **26**, 229–238.

Perini, G., Tepley, F. J., III, Davidson, J. P. & Conticelli, S. (2003). The origin of K-feldspar megacrysts hosted in alkaline potassic rocks from post-orogenic setting: a track for low-pressure processes in mafic magmas. *Lithos* **66**, 223–240.

Perugini, D. & Poli, G. (2001). Chaotic dynamics and fractals in magmatic interaction processes: a different approach to the interpretation of mafic microgranular enclaves. *Earth and Planetary Science Letters* **175**, 93–103.

Pinarelli, L., Poli, G. & Santo, A. P. (1989). Geochemical characterization of recent volcanism from the Tuscan Magmatic Province (Central Italy): the Roccastrada and San Vincenzo centers. *Periodica di Mineralogia* **58**, 67–96.

Poli, G. (1992). Geochemistry of Tuscan Archipelago granitoids: central Italy: the role of hybridization processes in their genesis. *Journal of Geology* **100**, 41–56.

Poli, G. & Tommasini, S. (1991). Model for the origin and significance of mafic microgranular enclaves in calc-alkaline granitoids. *Journal of Petrology* **32**, 657–666.

Poli, G., Frey, F. A. & Ferrara, G. (1984). Geochemical characteristics of the South Tuscany (Italy) Volcanic Province: constraints on lava petrogenesis. *Chemical Geology* **43**, 203–221.

Poli, G., Manetti, P. & Tommasini, S. (1989). A petrological review on Miocene–Pliocene intrusive rocks from Southern Tuscany and Tyrrhenian Sea (Italy). *Periodica di Mineralogia* **58**, 109–126.

Poli, G., Pecerillo, A. & Donati, C. (2002). Genesis of Miocene–Pliocene intrusive rocks from Tuscan Magmatic Province: implication on the structure of Appenninic lithosphere. *Memorie della Società Geologica Italiana, Special Volume* **1**, 129–139.

Principi, G. & Treves, B. (1984). Il sistema corso-appenninico come prisma d'accrezione. Riflessi sul problema generale del limite Alpi–Appennini. *Memoria della Società Geologica Italiana* **28**, 549–576.

Rocchi, S., Westerman, D. S., Dini, A., Innocenti, F. & Tonarini, S. (2002). Two-stage growth of laccoliths at Elba Island, Italy. *Geology* **30**, 983–986.

Sawka, W. N., Chappell, B. W. & Kistler, R. W. (1990). Granitoid compositional zoning by side-wall boundary layer differentiation: evidence from the Palisade Intrusive suite, Central Sierra Nevada, California. *Journal of Petrology* **31**, 519–553.

Serri, G., Innocenti, F. & Manetti, P. (1993). Geochemical and petrological evidence of the subduction of delaminated Adriatic lithosphere in the genesis of the Neogene–Quaternary magmatism of central Italy. *Tectonophysics* **223**, 117–147.

Shimizu, N. (1981). Trace element incorporation into growing augite phenocrysts. *Nature* **289**, 575–577.

Shimizu, N. & Le Roex, A. P. (1986). The chemical zoning of augite phenocrysts in alkaline basalts from Gough Island, South Atlantic. *Journal of Volcanology and Geothermal Research* **29**, 159–188.

Singer, B. S., Dungan, M. A. & Layne, G. D. (1995). Textures and Sr, Ba, Mg, Fe, K and Ti compositional profiles in volcanic plagioclase: clues to the dynamics of calc-alkaline magma chambers. *American Mineralogist* **80**, 776–798.

Smith, J. V. & Brown, W. L. (1988). *Feldspar Minerals. 1, Crystal Structures, Physical, Chemical and Microtextural Properties*. Heidelberg: Springer, 828 pp.

Sparks, R. S. J. & Marshall, L. (1986). Thermal and mechanical constraints on mixing between mafic and silicic magmas. *Journal of Volcanology and Geothermal Research* **29**, 99–124.

Sparks, R. S. J., Sigurdsson, S. & Wilson, L. (1977). Magma mixing: a mechanism for triggering acid explosive eruptions. *Nature* **267**, 315–318.

Stimac, J. A. & Wark, D. A. (1992). Plagioclase mantles on sanidine in silicic lavas, Clear Lake, California: implications for the origin of rapakivi texture. *Geological Society of America Bulletin* **104**, 728–744.

Taylor, H. P. & Turi, B. (1976). High-^{18}O igneous rocks from the Tuscan Magmatic Province, Italy. *Contributions to Mineralogy and Petrology* **55**, 33–54.

Tepley, F. J., Davidson, J. P. & Clynne, M. A. (1999). Magmatic interactions as recorded in plagioclase phenocrysts of Chaos Crags, Lassen Volcanic Center, California. *Journal of Petrology* **40**, 787–806.

Tepley, F. J., III, Davidson, J. P., Tilling, R. I. & Arth, J. G. (2000). Magma mixing, recharge and eruption histories recorded in plagioclase phenocrysts from El Chichon volcano, Mexico. *Journal of Petrology* **41**, 1397–1411.

Tepley, F. J., III & Davidson, J. P. (2003). Mineral-scale Sr-isotope constraints on magma evolution and chamber dynamics in the Rum layered intrusion, Scotland. *Contributions to Mineralogy and Petrology* **145**, 628–641.

Trevisan, L. (1951). La 55 riunione estiva della Società geologica Italiana. *Bolletino della Società Geologica Italiana* **70**, 435–470.

Trevisan, L. & Marinelli, G. (1967). Carta geologica dell'Isola d'Elba (scala 1:25 000). Pisa: Consiglio Nazionale delle Ricerche.

Van Bergen, M. J. & Barton, M. (1984). Complex interaction of aluminous metasedimentary xenoliths and siliceous magma; an example from Mt. Amiata (Central Italy). *Contributions to Mineralogy and Petrology* **86**, 374–385.

Vaniman, D. (1978). Crystallisation history of sector-zoned microcline megacrysts from the Godani Valley pluton, Nigeria. *Mineralogical Magazine* **42**, 443–451.

Vernon, R. H. (1984). Microgranitoid enclaves in granites—globules of hybrid magma quenched in a plutonic environment. *Nature* **309**, 438–439.

Vernon, R. H. (1986). K-feldspar megacrysts in granites—phenocrysts, not porphyroblasts. *Earth-Science Reviews* **23**, 1–63.

Vernon, R. H. (1990). Crystallisation and hybridism in microgranitoid enclave magmas: microstructural evidence. *Journal of Geophysical Research* **95**, 17849–17859.

Verplanck, P. L., Farmer, G. L., McCurry, M. & Mertzman, S. A. (1999). The chemical and isotopic differentiation of an epizonal magma body: Organ Needle Pluton, New Mexico. *Journal of Petrology* **40**, 653–678.

Waight, T., Dean, A. A., Maas, R. & Nicholls, I. A. (2000*a*). Sr and Nd isotopic investigations towards the origin of feldspar megacrysts in microgranular enclaves in two I-type plutons of the Lachlan Fold Belt, southeast Australia. *Australian Journal of Earth Sciences* **47**, 1105–1112.

Waight, T. E., Maas, R. & Nicholls, I. A. (2000*b*). Fingerprinting feldspar phenocrysts using crystal isotopic composition stratigraphy: implications for crystal transfer and magma mingling in S-type granites. *Contributions to Mineralogy and Petrology* **139**, 227–239.

Waight, T. E., Maas, R. & Nicholls, I. A. (2001). Geochemical investigations of microgranitoid enclaves in the S-type Cowra Granodiorite, Lachlan Fold Belt, SE Australia. *Lithos* **56**, 165–186.

Wark, D. A. & Stimac, J. A. (1992). Origin of mantled (rapakivi) feldspars: experimental evidence of a dissolution and diffusion-controlled mechanism. *Contributions to Mineralogy and Petrology* **111**, 345–361.

Watson, E. B. (1982). Basalt contamination by continental crust: some experiments and models. *Contributions to Mineralogy and Petrology* **80**, 73–87.

Westerman, D. S., Innocenti, F., Tonarini, S. & Ferrara, G. (1993). The Pliocene intrusions of the Island of Giglio. *Memoria della Società Geologica Italiana* **49**, 345–363.

White, A. J. R., Chappell, B. W. & Wyborn, D. (1999). Application of the restite model to the Deddick granodiorite and its enclaves—a reinterpretation of the observations and data of Maas *et al.* (1997). *Journal of Petrology* **40**, 413–421.

Wiebe, R. A. (1993). The Pleasant Bay layered gabbro–diorite, coastal Maine: ponding and crystallisation of basaltic injections into a silicic magma chamber. *Journal of Petrology* **102**, 461–489.

Wiebe, R. A., Smith, D., Sturm, M., King, E. M. & Seckler, M. S. (1997). Enclaves in the Cadillac Mountain granite (coastal Maine): samples of hybrid magma from the base of the chamber. *Journal of Petrology* **38**, 393–423.

Wolff, J. A., Ramos, F. C. & Davidson, J. P. (1999). Sr isotopic disequilibrium during differentiation of the Bandelier Tuff: constraints on the crystallisation of a large rhyolitic magma chamber. *Geology* **27**, 495–498.

Wyllie, P. J., Cox, K. G. & Biggar, G. M. (1962). The habit of apatite in synthetic systems and igneous rocks. *Journal of Petrology* **3**, 238–243.

Zellmer, G. F., Blake, S., Vance, D., Hawkesworth, C. & Turner, S. (1999). Plagioclase residence times at the two island arc volcanoes (Kameni Islands, Santorini, and Soufrière, St Vincent) determined by Sr diffusion systematics. *Contributions to Mineralogy and Petrology* **136**, 345–357.

Zellmer, G. F., Sparks, R. S. J., Hawkesworth, C. & Wiedenbeck, M. (2003). Magma emplacement and remobilization timescales beneath Montserrat: insights from Sr and Ba zonation in plagioclase phenocrysts. *Journal of Petrology* **44**, 1413–1431.

Zhang, Y., Walker, D. & Lesher, C. E. (1989). Diffusive crystal dissolution. *Contributions to Mineralogy and Petrology* **102**, 492–513.

Zorpi, M. J., Coulon, C., Orsini, J. B. & Cocirta, C. (1989). Magma mingling, zoning and emplacement in calc-alkaline granitoid plutons. *Tectonophysics* **157**, 315–329.